




Extended space charge and transport near ion-selective surfaces

Wei Liu, Yunfan Huang, Moran Wang^{*} 

Department of Engineering Mechanics, Tsinghua University, Beijing 100084, China

ARTICLE INFO

Keywords:

Electrokinetics
Microflow
Extended space charge layer
Electroconvective flow
Charge layer structure
Wave number

ABSTRACT

Electroconvective flow near ion-selective surfaces propels movements of ions and water, resulting in intricate phenomena influenced by fine interactions among fluid, voltage, and charge. However, the formation mechanism of the small number of cations in the extended space charge (ESC) near the ion-selective surfaces remains unclear. Herein, the origin of the small number of cations in ESC is investigated using a blockage-nanoslot-bulk structure. Direct numerical simulations of the fully coupled Poisson-Nernst-Planck and Navier-Stokes equations are presented for a blockage-nanoslot-bulk system under the influence of external fields. A strong electric field induced by ion flux is recommended as a critical factor for ESC formation based on transient analysis of the local fluid, voltage, and charges in the intermediate time. Once the ion flux exceeds the limiting current density, the induced strong negative electric field propels a small number of cations at the nanoslot-bulk interface to extend parallelly within a finite region, forming an ESC characterized by a localized peak charge structure. Furthermore, the self-similar extension of the ESC is determined based on variations in the ESC thickness, and the normalized structure of the space charge density was revealed by employing normalized coordinates, which were confirmed by direct numerical simulations. Finally, we showed the effect of the geometric structure on the vortex, demonstrating that the nanoslot structure significantly improves wave number prediction.

1. Introduction

When an external electric field is applied perpendicular to an ion-selective surface (or nanoslot), distinct ion-depleted and ion-enriched regions form on opposite sides of the surface. As the electric field strength increases, non-equilibrium ion transport near these surfaces intensifies, destabilizing the quiescent ion-depleted region and giving rise to rolling vortices—a phenomenon commonly referred to as electroconvection. It plays a crucial role in various fields such as wastewater treatment [1–4], biomedicine [5,6], electrokinetic micro-mixer [7,8], lab-on-a-chip [9,10], electrochemical devices [11,12], biological sensors [13], shock desalination [14,15], ion rectification [16,17], and colloidal systems [18–20].

The possible mechanisms of electroconvection are commonly classified into four categories: vortices driven by the extended space charge (ESC) layer [21], double layer [22–24], charge injection [25,26], and temperature patterns [27]. Here, we focus on electroconvection driven by the ESC. There exists abundant theoretical [28,29], computational [30–33], and experimental [34,35] research on electroconvection. The effect of voltage on fluid flow is a subject of universal interest. When the voltage exceeds a critical threshold (approximately 20 times the thermal

voltage), the flow transitions from a stable state without vortices to a state characterized by vortex rolling. This transition was successfully predicted by the linear stability theory [36]. With a further increase in the voltage, the electrostatic force destabilizes the steady vortex, causing a transition from regular vortices to irregular chaotic structures. The evolution exhibits self-similar characteristics and reveals a pattern of wavelength selection [35]. These electroconvective flow patterns [37–39] akin to Rayleigh–Bénard convection [40–43]. Subsequently, the system enters a nonlinear chaotic regime characterized by secondary instability [44]. These vortices exhibit chaotic transport characteristics, manifested as fluctuations in velocity and concentration [30,39].

Flow control is also a topic of the electroconvection. Some studies have been focused on investigating the impact of shear flow on electroconvection. These studies have revealed a shear sheltering effect, whereby an increase in the shear flow results in a significant vortex-height suppression [45–47], vortex state [48,49], vortex fluctuations [48], and vortex patterns [50,51]. In numerous applications, fluids exhibit non-Newtonian behavior, a phenomenon frequently observed in lithium batteries. A numerical investigation of the electrochemical processes within viscoelastic electrolytes revealed that flow instability is promoted by polymer stretching, which is contingent on the

^{*} Corresponding author.

E-mail address: mrwang@tsinghua.edu.cn (M. Wang).

<https://doi.org/10.1016/j.ijmecsci.2025.109933>

Received 13 October 2024; Received in revised form 12 December 2024; Accepted 1 January 2025

Available online 4 January 2025

0020-7403/© 2025 Elsevier Ltd. All rights reserved, including those for text and data mining, AI training, and similar technologies.

Weissenberg number [52]. The impact of a magnetic field on the electrochemical processes has been explored numerically [53]. Their findings revealed that the application of a magnetic field could modify the ion flux and electrochemical processes by inducing Lorentz forces, subsequently reducing the size of the flow structures. Moreover, current-induced membrane discharge can suppress the ESC and electroconvective flow through ionization [54]. Some studies have been focused on investigating electroconvective flows in circular geometries, and it was found that the curvature can enhance instability [23,55]. Some scholars have also shown that Rayleigh–Bénard flow [32,56–58] can be coupled with electroconvective flow, which exists in larger electrochemical devices. Karatay et al [32]. Found that when the direction of gravity and the direction of the electric field are consistent, when the Rayleigh number is very large, the electroconvective flow can be completely suppressed.

Despite significant advancements in understanding electroconvective flow and space-charge phenomena, the formation mechanism of the small number of cations in the ESC remains poorly understood. Existing studies have neither provided a systematic description, such as a the normalized structure of the space charge density, nor addressed the origin of this critical feature of ESC [21,35,48,49,52]. The relevant summary is as follows:

- (i) In membrane science, the Donnan potential at the membrane-resolution interface is widely acknowledged as a key factor in ion transport processes (Fig. 1(a)) [59]. However, recent findings, including our prior work [27,60], indicate the presence of significant periodic oscillations of the Donnan potential at the nanoslot-bulk interface. Such oscillations could serve as a potential mechanism for vortex formation, but this perspective has not yet been explored.
- (ii) Moreover, prior analyses of ESC formation have typically employed simplified structure, such as bulk region, which fail to capture the complexities of the bulk-nanoslot-bulk structure [61]. Notably, these approaches neglect the fluctuating nature of the Donnan potential and its impact on ion transport and charge redistribution (Fig. 1(b)). This limitation has constrained progress in understanding the mechanisms underlying ESC formation.
- (iii) In the field of electrokinetics, the electrical double layer (EDL), which arises from electrolyte polarization near charged surfaces, plays a central role in ion transport [62]. While it is generally recognized that ion flux contributes to ESC formation, as reported in previous studies [61,63], the physical origin of the small number of cations in the ESC has not been addressed. Specifically, Ref. [63] noted a connection between ESC and ion flux but did not provide a systematic explanation for the source of these cations (Fig. 1(c)).

To address these, this study aims to uncover the formation mechanism behind the small number of cations in the ESC. Herein, a three-layer blockage-nanoslot-bulk structure was designed, instead of the

traditional bulk-nanoslot-bulk [64,65]. Through a transient analysis of the local fluid, voltage, and charges in the intermediate time, we found that the ESC and vortices formed when the applied ion flux exceeded the limiting current density. Based on the analysis of the local driving forces, we elucidated the origin of the small number of cations in ESC. The analysis of the ESC formation revealed that the small number of cations in the ESC originated passively from the cations in the nanoslot. We also theoretically revealed the universal structure of the ESC and clarified the contributions of the Donnan potential and ESC to the vortex slip velocity. Finally, we discuss the improvement of the nanoslot structure in the quantitative prediction of the vortex wave number in the experiments.

The structure of this paper is outlined as follows: The first section introduces the theoretical background. In the second section, the computational model is developed, including the geometry, governing equations, and boundary conditions. The third section begins with the validation of the model. The results and discussion analyze the formation mechanism of ESC, the self-similar expansion, the vortex, and the effect of nanoslot on the wave number. Finally, the conclusions are presented in the last section.

2. Physical model and mathematical equations

In the blockage-nanoslot-bulk configuration studied here, the blockage structure plays a key role in enabling the EDL capacitive charging [66–70], thereby maintaining the local charge balance over intermediate timescales. To better understand the influence of this configuration, we compared the effects of the blockage-nanoslot-bulk structure with those of a classic monolayer structure (a bulk zone) on the flow.

Fig. 2 illustrates the schematic of ESC formation and electroconvective flow in blockage-nanoslot-bulk configuration, which involves ion transport, potential evolution, and fluid motion. Electroconvection can be described by the Poisson–Nernst–Planck equations and the incompressible Navier–Stokes equations.

$$\frac{\partial c_i}{\partial t} = D_i \nabla^2 c_i + D_i \frac{e}{k_B T} z_i \nabla \cdot (c_i \nabla \varphi) - \mathbf{U} \cdot \nabla c_i, \quad (1)$$

$$-\varepsilon \nabla \cdot (\nabla \varphi) = F(z_1 c_1 + z_2 c_2), \quad (2)$$

$$\frac{\partial \mathbf{U}}{\partial t} + \mathbf{U} \cdot \nabla \mathbf{U} = -\frac{1}{\rho} \nabla P + \frac{\mu}{\rho} \nabla^2 \mathbf{U} - \frac{F}{\rho} (z_1 c_1 + z_2 c_2) \nabla \varphi, \quad (3)$$

$$\nabla \cdot \mathbf{U} = 0, \quad (4)$$

where c_1 and c_2 are the cation and anion concentrations, respectively; e is the elementary charge; k_B is the Boltzmann constant; and T is the temperature. D_1 and D_2 are the diffusion coefficients of the cations and anions, respectively. \mathbf{U} is the fluid velocity. z_1 and z_2 are the valences of the cations and anions, respectively. In the Poisson equation, φ is the electric potential, $\varepsilon = \varepsilon_0 \varepsilon_1$ is the dielectric constant (ε_0 being the relative

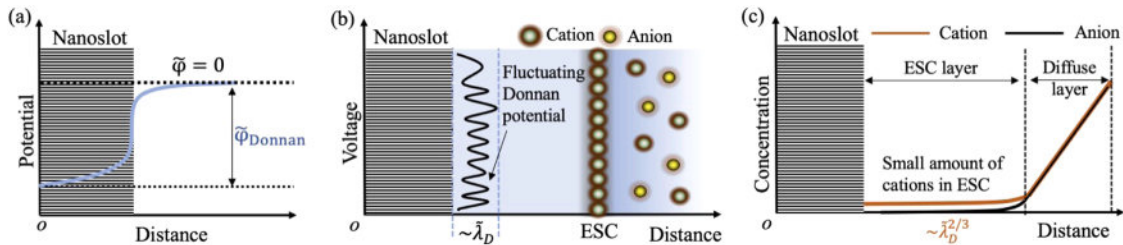


Fig. 1. Sketch of (a) the Donnan potential and (b) the fluctuating Donnan potential and the ESC. The fluctuating range of the Donnan potential is within $\sim \tilde{\lambda}_D$, and the ESC thickness is within $\sim \tilde{\lambda}_D^{2/3}$. (c) Ion concentration distribution. When the ion flux is much greater than the limiting current density j_{lim} , a broad non-zero cation concentration area is formed near the nanoslot-bulk interface, but the anion concentration is zero. This area is called the ESC layer, and the outer layer is called the diffuse layer.

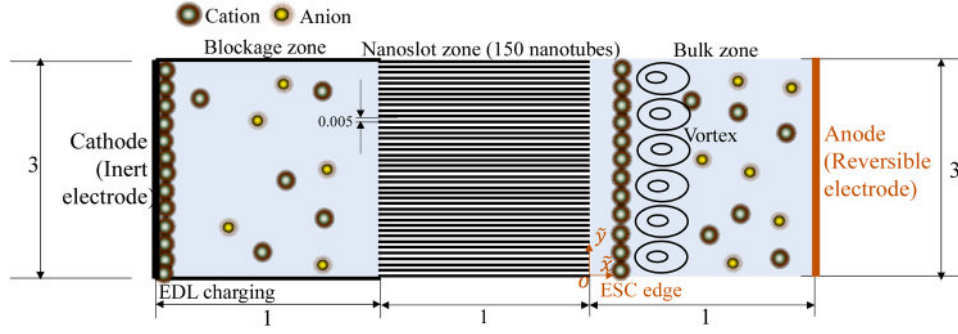


Fig. 2. The two-dimensional computational domain consists of three main zones: a blockage zone, a nanoslot zone, and a bulk zone. The nanoslot zone contains 150 rectangular nanochannels, which are uniformly arranged in parallel. Due to their dense arrangement, only a few nanochannels are shown schematically for clarity. The dimensionless sizes of the different zones are marked in the figure. In this study, the dimensionless Debye length is set to 0.001 [32,33,39], representing a 1-mM salt solution, with a reference characteristic length of 10 μm . This means that when the dimensionless size is 1, it corresponds to an actual size of 10 μm . The walls of the nanochannels are assumed to carry fixed negative charges. These charges cause the formation of overlapping EDLs within the nanochannels, leading to the development of Donnan potentials at the interface between the nanoslot zone and the surrounding solution. As a result, the nanoslot zone acts as a perfectly ion-selective region.

dielectric constant of the solution and ϵ_1 being the vacuum dielectric constant), and F is the Faraday constant. In the Navier–Stokes equations, ρ is the fluid density, P is the pressure, μ is the viscosity, and t is the time.

The spatial coordinates, fluid velocity, pressure, time, ion concentration, flux, and electric potential are non-dimensionalized using the microchannel length l_0 , diffusion velocity D_0/l_0 , diffusion time l_0^2/D_0 , bulk concentration c_0 , osmotic pressure $\mu D_0/l_0^2$, diffusion flux $D_0 c_0/l_0$, and thermal voltage $k_B T/e$, respectively. Here, D_0 represents the reference diffusion coefficient, which is selected as $10^{-9} \text{m}^2/\text{s}$ in this study. The following dimensionless forms of the Poisson–Nernst–Planck and Navier–Stokes equations can be obtained:

$$\frac{\partial \tilde{c}_i}{\partial \tilde{t}} = -\tilde{\nabla} \cdot \tilde{\mathbf{J}}_i = -\tilde{\nabla} \cdot (-\tilde{D}_i \tilde{\nabla} \tilde{c}_i - \tilde{D}_i \tilde{z}_i \tilde{c}_i \tilde{\nabla} \tilde{\varphi} + \tilde{\mathbf{U}} \cdot \tilde{c}_i), \quad (5)$$

$$-\tilde{\nabla}^2 \tilde{\varphi} = \frac{\tilde{z}_1 \tilde{c}_1 + \tilde{z}_2 \tilde{c}_2}{\tilde{\lambda}_D^2}, \quad (6)$$

$$\text{Re} \frac{\partial \tilde{\mathbf{U}}}{\partial \tilde{t}} + \text{Re} \tilde{\mathbf{U}} \cdot \tilde{\nabla} \tilde{\mathbf{U}} = -\tilde{\nabla} \tilde{P} + \tilde{\nabla}^2 \tilde{\mathbf{U}} - \tilde{\kappa} \frac{\tilde{z}_1 \tilde{c}_1 + \tilde{z}_2 \tilde{c}_2}{\tilde{\lambda}_D^2} \tilde{\nabla} \tilde{\varphi}, \quad (7)$$

$$\tilde{\nabla} \cdot \tilde{\mathbf{U}} = 0, \quad (8)$$

where c_1 and c_2 represent the dimensionless concentrations of the cations and anions, respectively; $\tilde{\mathbf{J}}_i$ denotes the dimensionless ion flux; \tilde{D}_i represents the dimensionless diffusion coefficients; \tilde{z}_i indicates the valence; $\tilde{\varphi}$ denotes the dimensionless electric potential; $\tilde{\mathbf{U}}$ indicates the dimensionless velocity; and \tilde{P} represents the dimensionless pressure. In this case, for simplicity, we consider $\tilde{D}_1 = \tilde{D}_2 = 1$ and $\tilde{z}_1 = -\tilde{z}_2 = 1$ [30, 39]. The dimensionless Debye length $\tilde{\lambda}_D = \sqrt{\epsilon k_B T / [e^2 c_0]} / l_0$ describes the ratio of the characteristic EDL thickness $\sqrt{\epsilon k_B T / [e^2 c_0]}$ to the channel size l_0 . Due to electroconvection having a weak sensitivity relation with the dimensionless Debye length, here we select $\tilde{\lambda}_D = 10^{-3}$ [32,33,39]. $\text{Re} = \frac{u_0 l_0 \rho}{\mu} = 0.001$ is the Reynolds number, where u_0 is the diffusion velocity. The electroconvective instability operates at a low Reynolds number, allowing the inertia term ($\text{Re} \frac{\partial \tilde{\mathbf{U}}}{\partial \tilde{t}} + \text{Re} \tilde{\mathbf{U}} \cdot \tilde{\nabla} \tilde{\mathbf{U}}$) in the Navier–Stokes equation to be neglected in direct numerical simulation (DNS) [30,39]. The dimensionless hydrodynamic coupling coefficient $\tilde{\kappa} = V_T^2 e / (\mu D_0)$ describes the influence of the physical properties of the electrolyte in the electrostatic force on the fluid. For common salt solutions (KCl), $\tilde{\kappa}$ does not vary extensively within the parameter space but remains a constant value. Considering a 1-mM KCl solution in the channel at a room temperature of $T = 300\text{K}$, the hydrodynamic coupling coefficient is a fixed

constant of $\tilde{\kappa} = 0.5$ [33,39].

To solve equations (2.5)–(2.8) numerically, the corresponding boundary conditions are required. The walls of the nanoslot were assumed to be impermeable to fluids and ions and uniformly charged with a negative charge density [11,71–75]. The boundary equations corresponding to the nanoslots are as follows:

$$(\tilde{D}_i \tilde{\nabla} \tilde{c}_i + \tilde{D}_i \tilde{z}_i (\tilde{c}_i \tilde{\nabla} \tilde{\varphi})) \cdot \mathbf{n} = 0,$$

$$\tilde{\mathbf{U}} = 0, \quad -\tilde{\nabla} \tilde{\varphi} \cdot \mathbf{n} = -l_0 \sigma / (\epsilon V_T), \quad (9)$$

where \mathbf{n} is the unit outward normal vector to the boundary surface. $-l_0 \sigma / \epsilon V_T$ describes the dimensionless normal electric field strength generated by the negative charge on the wall, which is normalized by the average electric field (V_T/l_0). Here, σ is defined as the charge density on the nanochannel wall. In this study, we use $-\tilde{\nabla} \tilde{\varphi} \cdot \mathbf{n} = 4000$.

At the blockage end (cathode), a no-flux, impermeable, no-slip boundary was considered, and the boundary conditions were as follows:

$$-\tilde{\nabla} \tilde{\varphi} \cdot \mathbf{n} = 0, \quad \tilde{\mathbf{U}} = 0, \quad (\tilde{D}_i \tilde{\nabla} \tilde{c}_i + \tilde{D}_i \tilde{z}_i (\tilde{c}_i \tilde{\nabla} \tilde{\varphi})) \cdot \mathbf{n} = 0, \quad \tilde{\varphi}_L = 0. \quad (10)$$

Here, $\tilde{\varphi}_L$ is the potential at the cathode (inert electrode).

When the ion flux is applied, the bulk end is connected to the reversible electrode. At the bulk end (anode), the concentrations of both the anions and cations are assumed to be identical, and there is an ion flux \tilde{j} across it. If the voltage is applied, the bulk end is connected to the inert electrode. The corresponding boundaries are as follows [76,77]:

$$\tilde{c}_1 = \tilde{c}_2 = 1, \quad (\tilde{D}_1 \tilde{\nabla} \tilde{c}_1 + \tilde{D}_1 \tilde{z}_1 (\tilde{c}_1 \tilde{\nabla} \tilde{\varphi})) \cdot \mathbf{n} = \tilde{j}. \quad (11)$$

$$\tilde{c}_1 = \tilde{c}_2 = 1, \quad \tilde{\varphi} = \tilde{\varphi}_R. \quad (12)$$

On calculating the effects of the flux boundary (11) and voltage boundary (12) on the ESC, we observed that, for the blockage-nanoslot-bulk structure, the ESC near the nanoslot-bulk interface depended only on the flux.

The finite element method was employed to solve the aforementioned dimensionless Navier–Stokes and Poisson–Nernst–Planck equations along with the boundary conditions. A quadrature mesh was used to discretize the nanoslot region. To accurately capture the overlapping double layers, the longitudinal mesh size within the double layers was set as $\mathcal{O}(0.1 \tilde{\lambda}_D)$. To capture the ESC layers at the nanoslot-bulk interface, a mesh with a count of $\mathcal{O}(10^2 \tilde{\lambda}_D)$ is deployed with localized refinement. Such a non-uniform mesh partition facilitates the precise capture of overlapping double layers, which results in ion-selective transport and electroconvection induced by the ESC layer. Furthermore, we verified the grid independence and found that the concentration and potential

distributions are nearly identical for grid sizes of $\mathcal{O}(0.01\tilde{\lambda}_D)$, $\mathcal{O}(0.05\tilde{\lambda}_D)$, and $\mathcal{O}(0.1\tilde{\lambda}_D)$. Therefore, the mesh size within the double layers in the nanoslot was set as $\mathcal{O}(0.05\tilde{\lambda}_D)$, which aids in effectively capturing statistical information of the concentration, electric field, and flow field. In our study, the formation mechanism of the ESC was explored by adjusting the ion flux. Based on the Ref. [61], we chose the range of $0 \leq \tilde{j} \leq \mathcal{O}(1)$. The height of the nanoslot was set such that it was consistent with the Debye length to ensure well-overlapped EDLs and improved ion selectivity in the nanochannel. Further simulation details can be found in our previous studies [23,46,49,60].

3. Results and discussion

Previous studies have extensively analyzed bulk-nanoslot-bulk structures, providing validation for validating our model. To confirm the accuracy of our simulation, we reproduced the ion concentration and voltage distribution in the nanoslot from Ref. [77], as shown in Fig. 3(a) and (b). The results closely match the reference data, demonstrating that the overlapping electrical double layers (EDLs) create a block-like cation concentration profile and steep voltage gradients at the nanoslot-bulk interface. These findings validate the ability of our DNS approach to accurately capture the nonlinear ion concentration and voltage distributions within nanoslots.

Fig. 3(c) provides a quantitative comparison between the results from DNS and the analytical solutions, showing excellent agreement. This agreement further validates the accuracy of the DNS approach. Additionally, the Donnan potential is observed to increase with increasing bulk ion concentration, consistent with theoretical predictions. This agreement establishes a reliable basis for the subsequent analysis of ESC.

3.1. Formation mechanism of ESC

In a traditional bulk-nanoslot-bulk structure, an increase in the external voltage causes an increase in the ion flux, resulting in intricate coupling effects at the nanoslot-bulk interface and making the elucidation of ESC mechanisms challenging. Consequently, irrespective of the voltage [78] or current [76] is applied, the ESC is induced near the nanoslot-bulk interface, see Table 1.

To address this issue, a blockage-nanoslot-bulk structure was proposed. Unlike the bulk-nanoslot-bulk configuration, the blockage-nanoslot-bulk structure offers a key advantage: it decouples the voltage and current, thereby ensuring that the formation of ESC near the

Table 1

Comparison of the electroconvective response near nanoslot-bulk interface to different loading type of electrode setups between the bulk (inert electrode)-nanoslot-bulk (inert electrode) structure and the blockage (inert electrode)-nanoslot-bulk (reversible electrode) structure.

Boundary Geometry condition Structure	Inert electrode with a voltage exceeding $20k_B T/e$	Reversible electrode with a current exceeding I_{lim}
Bulk-nanoslot-bulk	With ESC	With ESC
Blockage-nanoslot-bulk	Without ESC	With ESC

nanoslot-bulk interface depends solely on ion flux. Notably, the blockage in this model serves the critical function of capacitive charging within the EDL.

In a blockage-nanoslot-bulk structure, the blockage end serves as an inert electrode (platinum electrode), while the bulk end is connected to a reversible electrode. Under the influence of an external voltage, ion accumulation occurs at the blockage end, resulting in EDL capacitive charging. When the applied voltage is sufficiently high, intense polarization occurs at the blockage end, resulting in ESC formation near the blockage end, which is similar to the concentration polarization observed on metal surfaces. At this point, the ESC is absent near the nanoslot-bulk interface. The ion flux in the bulk region of the nanoslot reaches a saturation value of 0.19. However, when an ion current is applied, ions cross the nanoslot-bulk interface, creating a strong concentration gradient at the nanoslot-bulk interface and causing the ESC formation near the nanoslot-bulk interface. A slight EDL capacitive charging occurs at the blockage end, and there is no ESC; see Table 1 and Fig. 5(b).

In the blockage-nanoslot-bulk structure, applying a voltage at the bulk end initially generates a brief surge of capacitive current, followed by a steady decrease to smaller currents, as shown in Fig. 4(a). This behavior is similar to capacitor charging at the blockage end, which acts as an inert electrode. At this end, ions accumulate and charge the EDL, eventually reaching equilibrium. Strong ion concentration polarization occurs exclusively at the blockage end for sufficiently high applied voltages, as seen in the inset of Fig. 4(b), consistent with previous observations [54]. Calculations reveal that the ion current in the nanoslot-bulk region saturates at approximately 0.19, as shown in Fig. 4(b), below the limiting current of 1. Even when the applied voltage reaches 200 times the thermal voltage, no ESC forms near the

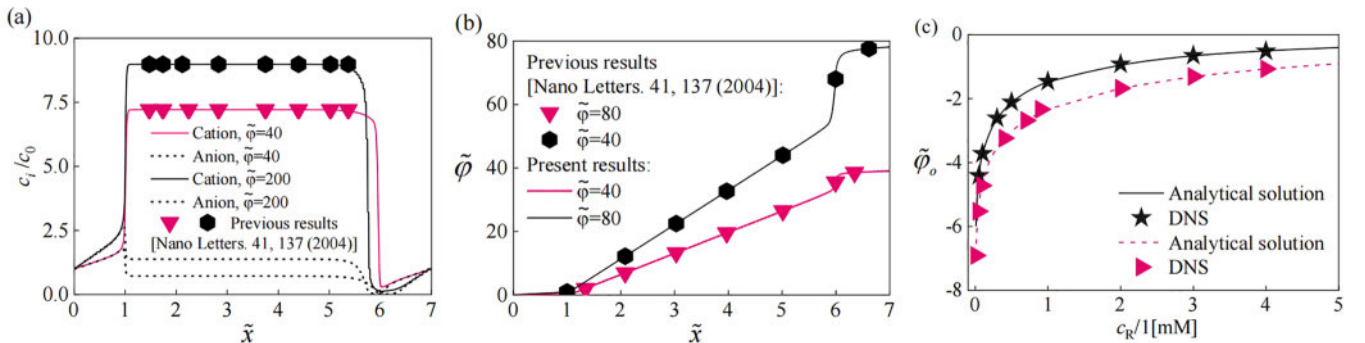


Fig. 3. Model validation. (a) Comparative verification of ion concentration and (b) voltage distribution in a single nanoslot, from which the scattered points are extracted. (c) Effect of concentration of right end (anode side) on Donnan potential. The solid line corresponds to $H = 5\text{nm}$, while the dashed line corresponds to $H = 2\text{nm}$. On neglecting the effect of the ESC, Ref. [60] derived an analytical solution of the Donnan potential at the nanoslot interface as $\tilde{\varphi}_0 = \left[\varphi_R + \frac{k_B T}{zF} \ln \left(\frac{\sqrt{(\sigma/(zFH))^2 + c_R^2} + \frac{\sigma}{zFH}}{c_R} \right) \right] / V_T$, where $\tilde{\varphi}_0 V_T$ represents the Donnan potentials at the left and right interfaces of the nanoslot, with $V_T = k_B T/e$ as the reference thermal voltage. φ_L and φ_R denote the potential at the left (cathode) and right (anode) ends, respectively. c_L and c_R denote the concentration of the left (cathode side) and right (anode side) ends, respectively. The bulk concentration is 1mM. Here, $\tilde{\varphi}_L = \tilde{\varphi}_R = 0$, $\tilde{c}_L = \tilde{c}_R$, and $\sigma = -1\text{mC/m}^2$.

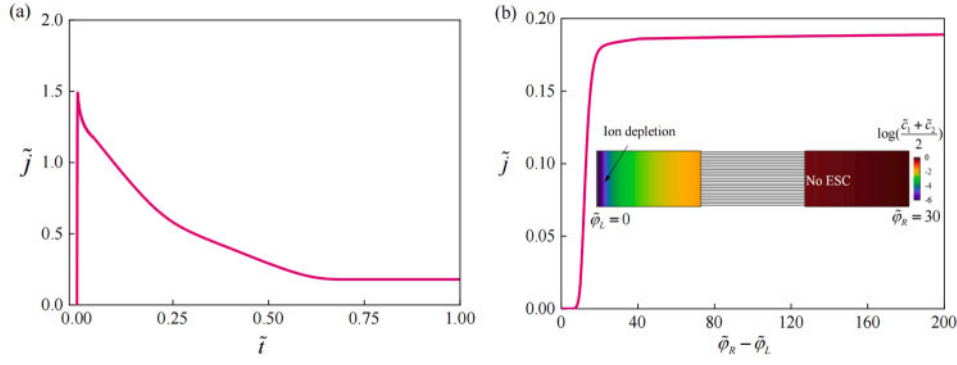


Fig. 4. EDL capacitive charging under the applied voltage. (a) Transient evolution of ion flux under voltage difference ($\tilde{\varphi}_R - \tilde{\varphi}_L = 30$) in the blockage-nanoslot-bulk structure. (b) Relationship between voltage and current in the blockage-nanoslot-bulk structure. The inset shows the distribution of salt concentration when the voltage difference is 30. The ESC formation was not observed near the nanoslot-solution interface; however, ion depletion was observed at the blockage end. Ion flux \tilde{j} was calculated by subtracting the temporal and spatial average of the anion horizontal flux from the cation horizontal flux.

nanoslot-bulk interface.

When voltage is applied, the presence of local depletion on the blockage end (inert electrode) leads to a nonlinear voltage distribution on the blockage end, as shown in Fig. 5(d). However, when a current is applied, the presence of slight capacitive transport on the blockage results in the absence of steep voltage gradients, as shown in Fig. 5(d). When a current is applied from the bulk end (reversible electrode), ion current crosses the nanoslot-bulk interface and undergoes slight capacitive charging at the blocking end. Therefore, the state of EDL capacitive charging at the blockage end is the key to achieving decoupling voltage and current. Ion current crosses the nanoslot-bulk interface and undergoes slight capacitive charging at the blocking end, as shown in Fig. 5(b). Based on the analysis above, the function of the blockage end (inert electrode) is to regulate the extent of EDL charging, thereby maintaining the steady state and achieving the current decoupled from voltage.

In the blockage-nanoslot-bulk structure, the ESC was induced near the nanoslot-bulk interface only when an ion flux was applied, as illustrated in Fig. 5(a) and (b). However, when applying a voltage drop, there is no induced ESC near the nanoslot-bulk interface, and the Donnan potential at this interface aligns with the theoretical predictions, suggesting the absence of an ESC (Fig. 5(c)). Therefore, the physical mechanism of the ESC originates from the strong negative electric field induced by the ion flux crossing the nanoslot-bulk interface. On calculating the parameter space spanned by the ion current (ion flux), it is observed that the ESC is triggered only when the ion flux (\tilde{j}) surpasses the limiting current ($\tilde{j}_{limiting} = 1$). The limiting current is defined as the saturation value of the ion current (flux) in the one-dimensional scenario [61].

To elucidate the source of the cation concentration within the ESC, we provide a detailed analysis of ion migration mechanisms during its formation. Fig. 5(a) offers a comprehensive depiction of the ion transport processes at the nanoslot-bulk interface. The presence of a small number of cations within the ESC is attributed to their migration under the influence of a strong negative electric field generated by the ion flux crossing the nanoslot-bulk interface. This electric field facilitates the parallel migration of cations toward the anode, as shown in Figs. 5(a) and 6(a). The Donnan potential prevents anions from crossing the nanoslot-bulk interface, conferring ion-selective characteristics to the nanoslot. As a result, one of the key factors contributing to ESC formation is the Donnan potential.

Simultaneously, the strong negative electric field (Fig. 5(d)) drives a small number of anions near the nanoslot-bulk interface into the nanoslot, contributing to the local redistribution of ions. These processes form a region with a high, non-zero charge density confined between the nanoslot-bulk interface and the diffuse layer, characteristic of the ESC. This region exhibits a distinctive peak structure within the charge

density profile of the ESC. Additionally, the ion flux-induced Donnan potential deviates from theoretical predictions, indicating the significant contribution of the ESC to the overall potential distribution, as illustrated in Fig. 5(e). Based on the above analysis, we recommend that ESC is caused by Donnan potential and strong electric fields induced by ion flux. Furthermore, our theoretical derivation indicates that the Donnan potential and ion flux are the primary contributions to the formation of the ESC.

3.2. Dynamic and structural characteristics of ESC

The ESC layer differs from the EDL structure governed by the classical Boltzmann distribution and exhibits distinct spatial distribution characteristics. Within the ESC layer, the charge density increases with distance, reaching a local peak. However, outside the ESC layer, the charge density decays rapidly with distance. With increasing flux, the ESC extends outward, forming a self-similar structure in the intermediate time. Based on theoretical analysis, we obtain the equation for charge evolution in transient state. For detailed derivation process, refer to the Appendix.

For the diffuse layer ($\tilde{x}_{ESC} < \tilde{x} < 1$), the space-time distribution of the space charge $\tilde{q}_{DL1}(\tilde{x}, \tilde{t})$ is as follows:

$$\tilde{q}_{DL1}(\tilde{x}, \tilde{t}) = -\tilde{\lambda}_D^2 \frac{d^2 \left[\int_{\tilde{x}_{ESC}}^{\tilde{x}} \frac{\tilde{j}}{2c_{DL}(x,t)} d\tilde{x} \right]}{d\tilde{x}^2}. \quad (13)$$

For the ESC layer ($0 < \tilde{x} < \tilde{x}_{ESC}$), the space charge $\tilde{q}_{ESC}(\tilde{x}, \tilde{t})$ is distributed as follows:

$$\tilde{q}_{ESC}(\tilde{x}, \tilde{t}) = -\tilde{\lambda}_D^2 \frac{d^2 \tilde{\varphi}_{ESC}(\tilde{x}, \tilde{t})}{d\tilde{x}^2} = -\frac{\tilde{\lambda}_D \sqrt{\tilde{j}}}{2\tilde{\lambda}_D} (\tilde{x}_{ESC}(\tilde{t}) - \tilde{x})^{-1/2}. \quad (14)$$

During intermediate times, the dynamic evolution of the space charge depends primarily on the extension of the ESC peak position ($\tilde{x}_{ESC}(\tilde{t})$), as indicated in Eq. (14). Hence, Fig. 6 shows that the ESC, characterized by its peak structure of the space charge density, exhibits a self-similar expansion towards the right.

We also derive a universal charge layer structure when the system reaches a steady state. More derivation details are given in the Appendix.

$$\tilde{c}_1 - \tilde{c}_2 = \alpha(\tilde{j}_1)^{0.5} \tilde{\lambda}_D, \quad (15)$$

$$\left[\tilde{x}_{ou} - \tilde{x} / \left(\frac{\sqrt[3]{9}}{2} \tilde{\lambda}_D^{\frac{2}{3}} (\tilde{j}_1)^{\frac{1}{3}} (\Delta\tilde{\varphi} - \tilde{\varphi}_{Donnan})^{\frac{2}{3}} \right) \right]^{-0.5}$$

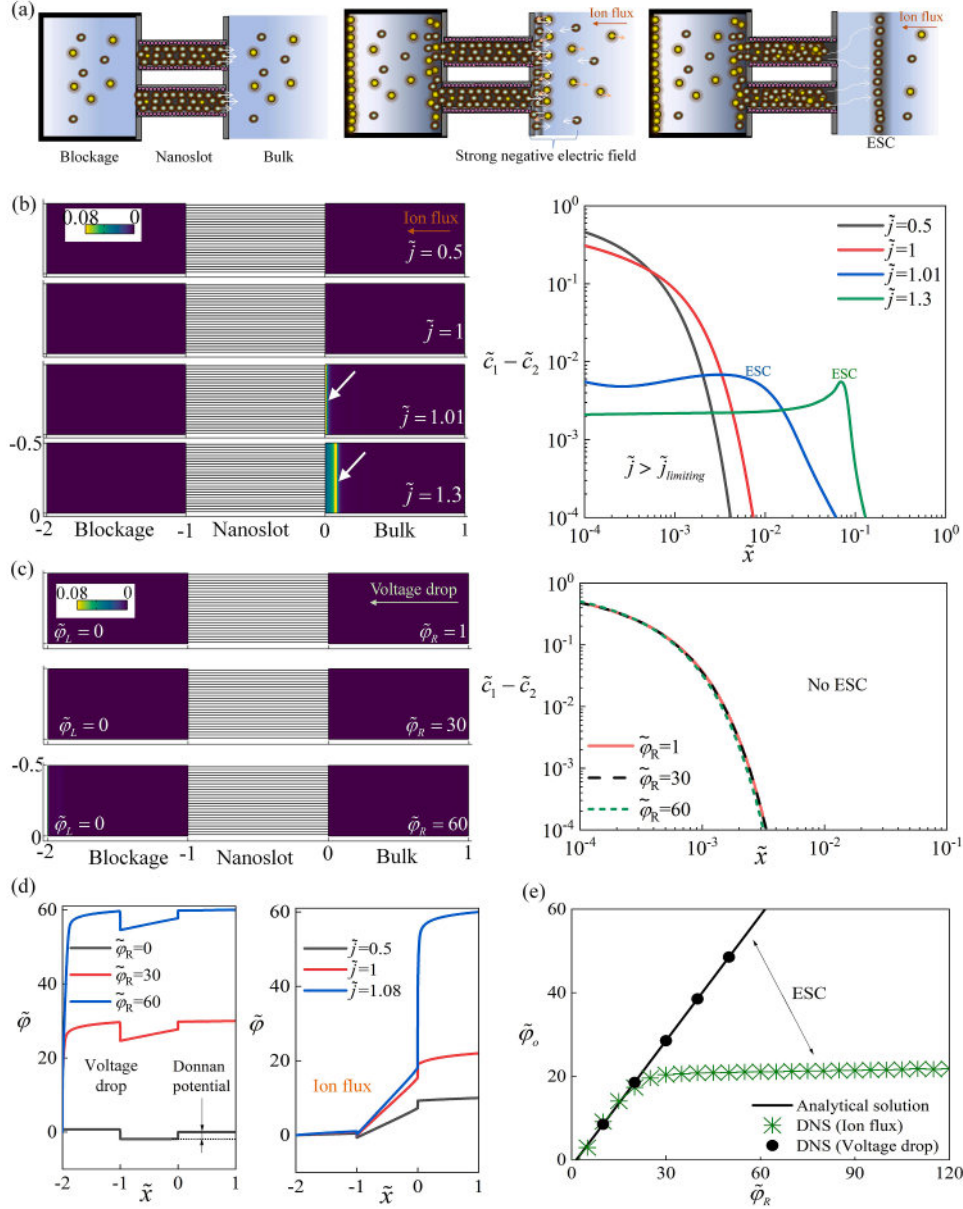


Fig. 5. Formation of the small number of cations in ESC. (a) Schematic of the strong negative electric field driving ion migration. A small number of cations near the nanoslot interface move into the bulk, creating a high-charge-density region, the ESC, between the nanoslot-bulk interface and the diffuse layer, forming a localized peak structure. Large spheres represent cations, and the small spheres represent anions. (b) Effect of the ion flux on the space charge density. (c) Effect of the voltage drop on the space charge density. (d) Effect of voltage drop and ion flux on the voltage distribution. (e) Effect of voltage drop and ion flux on Donnan potential. The theoretical curve is drawn using $\tilde{\varphi}_o = \left[\varphi_R + \frac{RT}{zF} \ln \left(\left(\sqrt{(\sigma/(zFH))^2 + c_R^2} + \frac{\sigma}{zFH} \right) / c_R \right) \right] / V_T$. With an increase in the ion flux, the Donnan potential deviates from theoretical predictions. The data here are all statistically analyzed under the scenario of intermediate time ($\tilde{t} = 1$).

$$\tilde{c}_1 - \tilde{c}_2 = \beta \tilde{\lambda}_D^2 \cdot \left[\tilde{x}_{ou} - \tilde{x} / \left(\frac{\sqrt[3]{9-2}}{2} \tilde{\lambda}_D^3 (\tilde{j}_1)^{\frac{1}{3}} (\Delta\tilde{\varphi} - \tilde{\varphi}_{Donnan})^{\frac{2}{3}} \right) \right]^{-2} \quad (16)$$

where α and β are fixed fitting coefficients.

$$\tilde{c}_1 - \tilde{c}_2 \sim \tilde{X}^{-\frac{1}{2}} = \left[\tilde{x}_{ou} - \tilde{x} / \left(\frac{\sqrt[3]{9-2}}{2} \tilde{\lambda}_D^3 (\tilde{j}_1)^{\frac{1}{3}} (\Delta\tilde{\varphi} - \tilde{\varphi}_{Donnan})^{\frac{2}{3}} \right) \right]^{-1/2} \quad (17)$$

$$\tilde{c}_1 - \tilde{c}_2 \sim \tilde{X}^{-2} = \left[\tilde{x}_{ou} - \tilde{x} / \left(\frac{\sqrt[3]{9-2}}{2} \tilde{\lambda}_D^3 (\tilde{j}_1)^{\frac{1}{3}} (\Delta\tilde{\varphi} - \tilde{\varphi}_{Donnan})^{\frac{2}{3}} \right) \right]^{-2} \quad (18)$$

where \tilde{x}_{ou} is the normalized thickness of the space charge layer.

On neglecting the pre-scaling factor, it can be determined that the space charge density has two universal scaling exponents that decay with the space position. We recast our DNS data using \tilde{X} as the horizontal axis, thus confirming the normalized structure of the space charge density with distance \tilde{X} (Fig. 7). The value of $\tilde{\varphi}_{Donnan}$ is obtained from the DNS and approaches a saturation value of approximately 21 as the ion flux increases. Therefore, based on the existing research [63], we confirmed the universality of the charge density decay scaling, and the normalized structure of the space charge density was given.

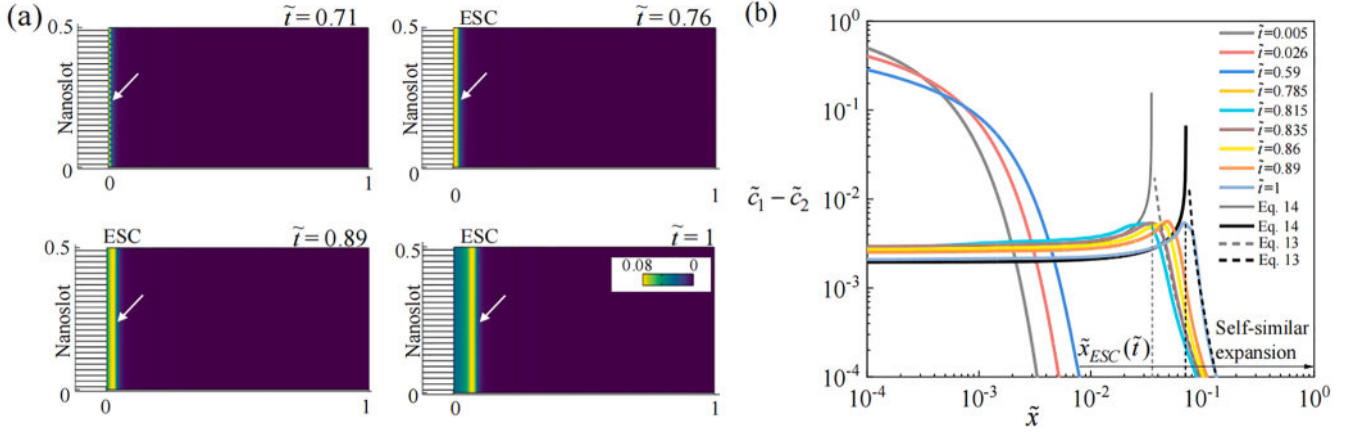


Fig. 6. Self-similar dynamics of ESC in the intermediate time. (a) Spatiotemporal evolution of space charge. The analysis also indicates that a small amount of cation concentration in ESC originates from cations at the nanoslot interface. (b) Self-similar extension of ESC in the intermediate time. The dynamic of the space charge is governed by the ESC peak position. Consequently, the ESC, distinguished by its peak structure, demonstrates a self-similar expansion to the right. Here, $\tilde{j} = 1.3$ and $\tilde{t} = 1$.

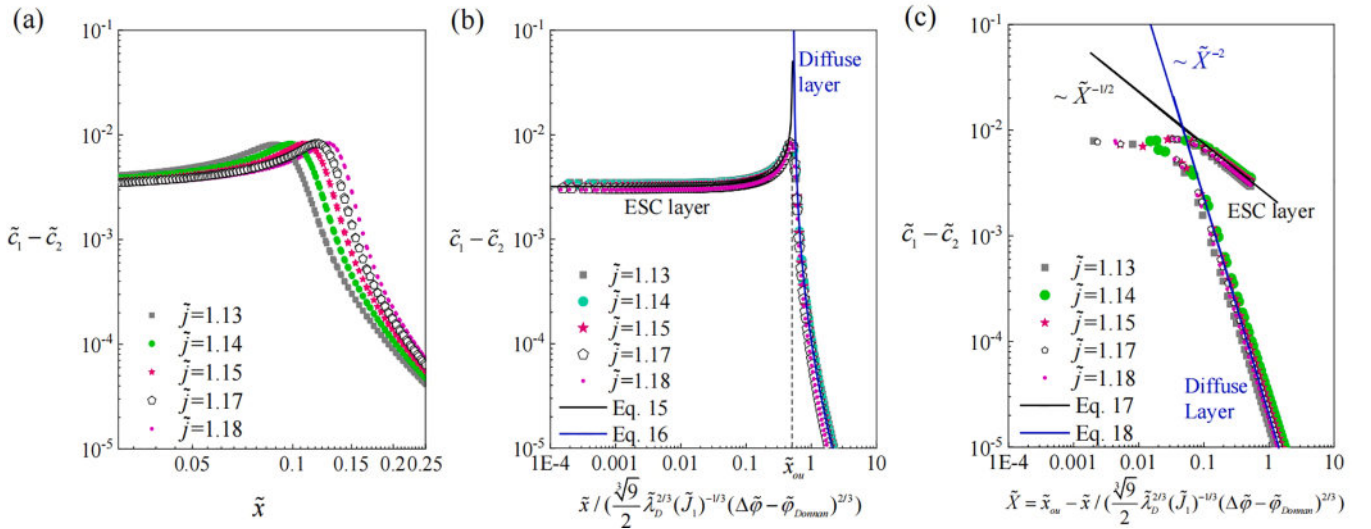


Fig. 7. Normalized structures of ESC in the intermediate time. (a) Dispersed space charge layer structure. (b) Normalized structure of space charge layer. The ESC structure is observed when located within \tilde{x}_{ou} , while the diffuse structure is observed beyond \tilde{x}_{ou} . (c) Charge density scaling. The two identifiable scaling regimes align with the ESC layer and diffuse layer, respectively. Data points are obtained from the DNS, while the solid lines depict the theoretical equations. Within the ESC layer, the charge exhibits an asymptotic decay scaling of $-1/2$, while in the diffuse layer (This term is suggested by the review [61]), the charge density decays with a power-law relation of -2 as the distance \tilde{X} increases (Fig. 7(c)). These charge density scalings are consistent with the Ref. [63]. The data are all analyzed in the intermediate time ($\tilde{t} = 1$).

3.3. Fluctuating Donnan potential and ESC contribution to vortex slip velocity

The periodic oscillation of the Donnan potential at the nanoslot-bulk interface may serve as a mechanism for the formation of electroconvection, which requires further validation. Fig. 8 (a) and (b) show the spatiotemporal evolution of the space charge, streamlines, and ion concentration. The extension of the ESC induced by the ion flux is observed, accompanied by the formation of electroconvection.

To reveal the mechanism behind the formation of electroconvection, i.e. to clarify whether it is governed by the Donnan potential or the ESC, we plotted the voltage distribution at the nanoslot-bulk interface, as shown in Fig. 8(c). Indeed, a significant amount of periodic fluctuation exists in the potential at the nanoslot-bulk interface, which is linearly correlated with the number of nanoslots. Twenty-five nanoslots induce 25 cycles of potential oscillations, thus generating many periodic and

strong electric fields at the nanoslot-bulk interface, which could potentially trigger vortex formation. However, the transient results of the flow and concentration fields indicate that 25 small-scale vortices are not observed near the nanoslot-bulk interface. A regular pair of vortices was observed; therefore, the Donnan potential at the nanoslot-bulk interface did not comprise the mechanism of electroconvection. The key observation is that the effective range of the periodic fluctuation in the Donnan potential is limited and decays rapidly with increasing distance. To investigate this further, the potential distribution was extracted by considering cross sections at different distances from the nanoslot-bulk interface. The effective range of the oscillating potential was smaller than the thickness of the ESC layer, thus indicating that the Donnan potential was not the driving force behind electroconvection. In particular, the effective fluctuation range of the Donnan potential extends to approximately 0.01 ($\mathcal{O}(\tilde{\lambda}_D)$) within the distance from the nanoslot-bulk interface, while the location corresponding to the peak of

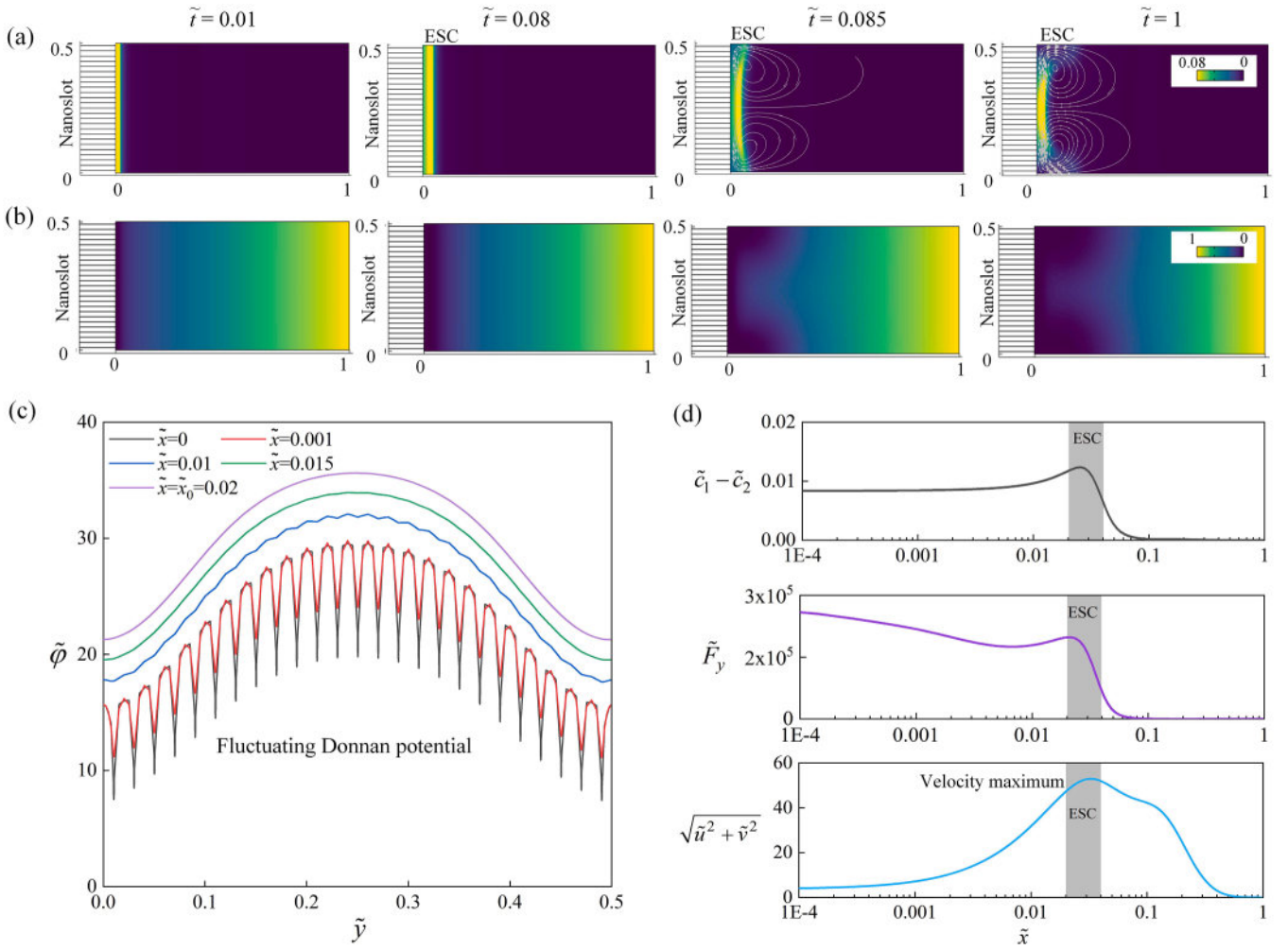


Fig. 8. Fluctuating Donnan potential and ESC contribution to slip velocity in blockage-nanoslot-bulk structure. (a) Spatiotemporal distribution of space charge ($\tilde{c}_1 - \tilde{c}_2$) and flow streamlines. (b) Spatiotemporal evolution of salt concentration $(\tilde{c}_1 - \tilde{c}_2)/2$. (c) Distribution of fluctuating potentials near the nanoslot-bulk interface. (d) Characteristics of horizontal distribution of space charge ($\tilde{c}_1 - \tilde{c}_2$), tangential volume forces (\tilde{F}_y), and velocity ($\sqrt{\tilde{u}^2 + \tilde{v}^2}$). The body force at the ESC edge is aligned with the slip velocity and ESC peak position, thus indicating that the ESC is the key vortex driving mechanism. Nanoscale vortices are absent at the nanoslot interface because the ESC layer, characterized by strong electric fields, has a thickness significantly exceeding that of the EDL. Here, $\tilde{j} = 1.1$ and $\tilde{t} = 1$.

the ESC is at $\tilde{x}_0 \approx 0.02$. This suggests that the range of impact of the Donnan potential did not reach the ESC layer. Based on the above analysis, the Donnan mechanism for electroconvection was ruled out, and the tangential slip velocity of the vortex did not act at the nanoslot-bulk interface, but only reached the inner edge of the ESC.

Next, we confirm the electroconvection mechanism of the ESC. On examining the distributions of space charge ($\tilde{c}_1 - \tilde{c}_2$), tangential volume forces (\tilde{F}_y), and velocity ($\sqrt{\tilde{u}^2 + \tilde{v}^2}$), evidence of the ESC mechanism was obtained. The local peaks of the ESC, tangential volume forces, and slip velocity coincide, as shown in Fig. 8 (d). If the slip velocity of the vortices originates from the oscillating Donnan potential, the electric field volume forces associated with the interface Donnan potential overcome the viscous forces driving the fluid motion, thus resulting in a slip velocity consistent with the position of the Donnan potential. However, the DNS results did not support this perspective. The slip velocity aligns with the position of the ESC layer, indicating that the ESC is the sole mechanism driving the vortex, as shown in Fig. 8(d). The oscillating Donnan potential at the interface provides local disturbances that serve as perturbations in the development of the flow instability. The counterclockwise-rotating vortices near the ESC are accompanied by corresponding perturbations in the salt-concentration field. Owing to the low Ohmic resistance of the high-concentration region, it exhibits

relatively uniform potential and, therefore, lower electric fields. Furthermore, examination of the electric field around the closed streamlines revealed the presence of a tangential electric field induced near the nanoslot-bulk interface. This tangential electric field acts within the ESC layer, which is consistent with the DNS observations. When the tangential electric field overcomes the viscous forces, it results in the overall growth of the perturbed vortices, eventually forming vortex structures at the edge of the ESC, as shown in Fig. 8(a). Thus, the strong tangential electric field within the ESC operates as a positive feedback mechanism and promotes vortex formation. The slip velocity of the vortices triggered at the ESC edge confirms the ESC rather than the fluctuating Donnan potential (Fig. 8 (c) and (d)).

3.4. Effects of nanoslot structure on flow pattern

We analyze the effect of the structure on the flow. Eq. (19) is used for the analysis of a single-layer structure (a bulk zone). Fig. 9 presents a quantitative comparison of the effects of the geometric structure on the flow. In the early stages, the membrane surface triggers a multitude of small-scale vortices. As time progresses, these small-scale vortices became unstable under the influence of localized concentration disturbances. They evolve from small-scale vortices into larger vortices, with the maximum vortex height being comparable to the channel height.

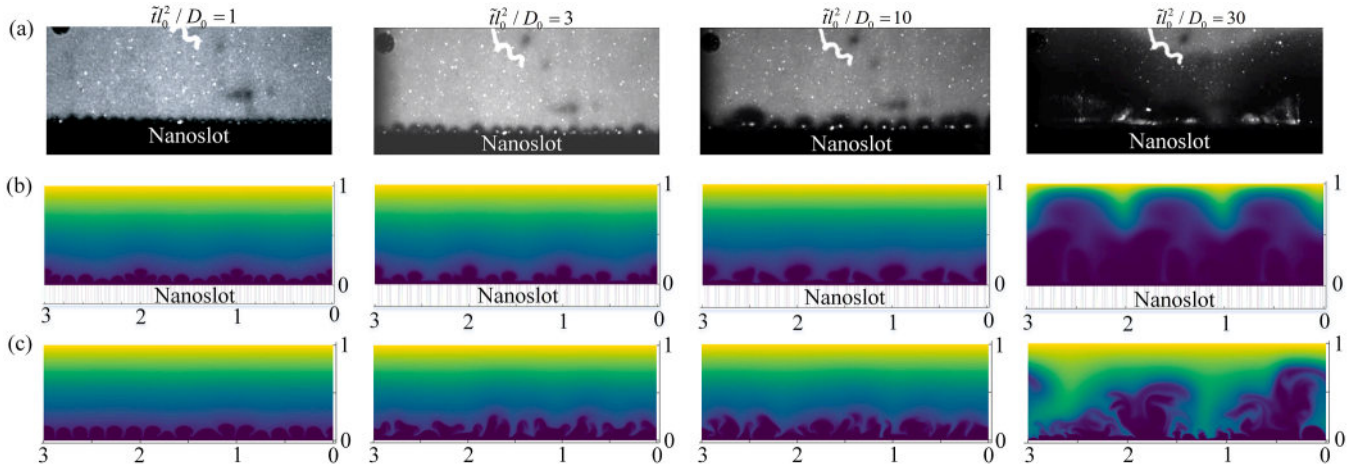


Fig. 9. Flow pattern. (a) Instantaneous snapshot of the experiment [78]. Simulation results were calculated using (b) the three-layer structure (nanoslot) and (c) classical single layer (fixed membrane concentration). The quantitative comparison comprises an assessment of the impact of the nanoslot on the flow prediction based on the flow pattern, thus indicating that the nanoslot structure agrees well with the flow pattern prediction. Here, $\tilde{j}=11$.

From a qualitative perspective, both boundary conditions captured the vortex structure; however, the flow structure differed. From the perspective of the wave number, ESC structure, and voltage distribution, the effects of the two types of structures on the flow prediction were quantitatively compared (Fig. 9(a)–(c)).

$$\tilde{c}_1 = 2, (\tilde{\nabla}\tilde{c}_2 + \tilde{z}_2(\tilde{c}_2\tilde{\nabla}\tilde{\varphi})) \cdot \mathbf{n} = 0. \quad (19)$$

A quantitative comparison of the wave numbers is presented, wherein the temporal evolution of the wave number k can be described by the following equation [78]:

$$k = \frac{8\pi}{5\sqrt{2D_0t}} \sim t^{-1/2}. \quad (20)$$

The measurement strategy for the vortex wave numbers has been detailed in previous studies. [78]. Experimental investigations demonstrated that particles near the nanoslot-bulk interfaces were swiftly captured within a sufficiently short temporal scale, facilitating a strategy for vortex wavelength selection. This phenomenon becomes evident from the increase in brightness at the stagnation points before the completion of the first observable annihilation–creation sequence of the array vortices.

To be consistent with the experiments [78], we used a KCl solution.

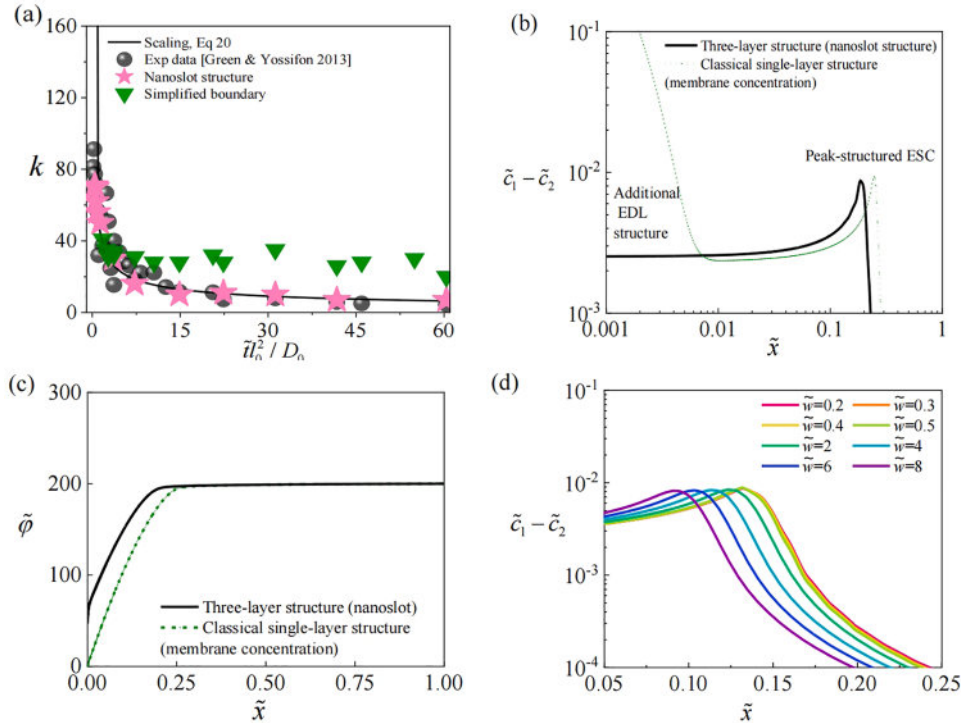


Fig. 10. Effect of the three-layer structure (nanoslot) and classical single layer (membrane concentration) on (a) the wave number, (b) space charge layer structure, and (c) voltage distribution. (d) Effect of nanoslot length \tilde{w} on the ESC structure. Compared with the classical single-layer, the nanoslot structure exhibits significant differences in the analysis of the ESC structure and voltage distribution. The Ref. [61] shows that, when the vortex is in a chaotic state, the wave number of the vortex depends mainly on time and has a weak sensitivity to the voltage and the dimensionless Debye length [32].

In the simulation of this paper, the geometry of the nanochannel is a two-dimensional rectangle, the length of the nanoslot region is 1 (10 μm), and the distance between the upper and lower walls of the nanochannel is 0.005 (5 nm), which can ensure sufficient overlap of the EDL. In the experiment [78], the length and depth of the nanoslot region are 0.35 mm and 190 nm, respectively. The experiment can be considered to comprise a quasi-two-dimensional structure because it has a low depth [78]. Our analysis indicates that the nanoslot length \tilde{w} has a negligible effect on the ESC, as demonstrated in Fig. 10(d). Consequently, the influence of the nanoslot region length on the vortex dynamics is minimal and can be disregarded. Previous studies [61] have shown that when the dimensionless voltage difference reaches 120, the vortex is already in a completely chaotic state. We selected the case in which the voltage decreases between the nanoslot and the bulk end were 200 (the ion flux was 11) to discuss the comparison between the three-layer and single-layer structures.

To determine the wave number (k) of the depletion regions, we first count the number of ion-depleted regions in instantaneous flow snapshots and calculate their average length, which corresponds to the wavelength ($\lambda = 2\pi/k$) of a single vortex pair. The wavelength is identified by measuring the lateral width of the plume within the vortex depletion region. Theoretical predictions suggest that the fully developed vortex wavelength ranges from 0.7 to 1.2 [21], whereas experimental observations indicate a wavelength of approximately 1.25 [78]. The wavelength calculated based on the three-layer structure was approximately 1, while that calculated using the simplified boundary varied widely, ranging from approximately 0.1 to 1.3. These findings suggest that predictions based on the Donnan boundary closely align with experimental observations. Therefore, wave numbers predicted from the three-layer structure closely matched experimental data, whereas predictions from the classical single-layer structure (with fixed membrane concentration) deviated. This discrepancy arises due to the presence of numerous small-scale vortices, which elevate the wave numbers, as illustrated in Fig. 10(a).

The calculations under the ion flux (the ion flux was set to 11) for both the simplified single-layer structure (with simplified boundaries) and the three-layer structure (including a nanoslot zone) have been extracted. Fig. 10(b)-(c) illustrate the respective distributions of the space charge and voltage. It is evident that the three-layer structure, incorporating the nanoslot, does not capture the double layer near the nanoslot-solution interface. Conversely, the simplified single-layer structure exhibits a distinct double-layer structure. Due to the presence of the EDL, a portion of the voltage is dropped across it. Consequently, calculations based on the simplified single-layer structure yield a larger voltage drop, approximately 200. In contrast, calculations based on the three-layer structure result in a relatively smaller voltage drop, approximately 140. Based on the above analysis, the electric field volume force within the ESC layer is greater for the simplified single-layer structure. However, for the three-layer structure, the electric field volume force within the ESC layer is smaller. Therefore, the electric field force calculated for the single-layer structure is larger, resulting in a smaller vortex size excited, or equivalently, a larger vortex wave number as depicted in Fig. 10(a). Finally, we discuss the effect of the nanoslot length \tilde{w} on the ESC (Fig. 10(d)). As the nanoslot length increases, the ESC tends to shrink. However, the ESC tends to expand as the voltage increases.

4. Conclusions

To reveal the ESC formation mechanism near the ion-selective surfaces, we designed a microfluidic channel with a blockage-nanoslot-bulk

configuration rather than a classical bulk-nanoslot-bulk formulation. Based on the theory of Rubinstein and Zaltzman, through the DNS and theoretical analyses, in the intermediate timescale, we found the formation mechanism of the ESC is attributed to the strong negative electric field induced by the ion flux, and the cations within the ESC originate from the cations of the ion-selective surface.

Using the normalized coordinate, the normalized structure of the charge density was revealed. Furthermore, The contributions of the ESC and Donnan potential to vortices were discussed, and it was found that the ESC is the key factor that induces vortices, while the Donnan potential ensures ion selectivity. Finally, The effects of the nanoslot structure on flow are discussed. Compared with the calculations based on the classical single-layer (fixed membrane concentration) structure, the results obtained from the three-layer structure with nanoslot calculations demonstrate better agreement with the experimental data. This improvement is credited to accurate predictions for precise insights into the local ESC and voltage distribution structures.

These results enhance the understanding of the ESC and electro-convection near ion-selective surfaces (nanochannels, reversible electrodes, and selective membranes), thus facilitating a quantitative understanding of the charge density and flow structure statistics. The blockage-nanoslot-bulk structure proposed in this study is expected to aid in realizing the simulation of more complex brain neuron signals. Because of the complexity of brain neurons, blockage (dead-end) areas often exist at neuron connections[81–84]. Further consideration of the blockage-nanoslot-bulk structure is expected to aid in simulating and designing applications of complex ionic neuromorphic signaling.

Due to the exceptionally slow capacitive charging under high voltage conditions [70,85], vortices are initiated within a few seconds, and chaotic fluctuations emerge, approximately reaching a statistically steady state [61]. As a result, it is challenging to extend the simulations in this study over long durations. Therefore, our simulations are confined to an intermediate timescale, and the steady-state limit of the system under long-term conditions remains unexplored, which is a limitation of the hypothetical scenario of this work. Following Ref. [61], the dimensionless simulation time is typically chosen as $\mathcal{O}(0.1) \sim \mathcal{O}(1)$ to represent intermediate times. The nanoslots, acting as charge buffers, continuously affect the balance between the electric field and space charge during the transient time. In future work, we will explore the system long-term response through both experimental and theoretical approaches.

CRedit authorship contribution statement

Wei Liu: Writing – original draft, Investigation. **Yunfan Huang:** Writing – review & editing, Validation. **Moran Wang:** Writing – review & editing, Supervision, Conceptualization.

Declaration of competing interest

The authors declare that they have no known competing financial interests or personal relationships that could have appeared to influence the work reported in this paper.

Acknowledgements

The authors express their sincere gratitude for the financial support provided by the NSF of China (No. 12272207), China Postdoctoral Science Foundation (No. 2023M741970), and the Postdoctoral Fellowship Program of CPSF (No. GZB20230361).

Appendix

Based on Poisson's equation, the spatiotemporal distribution of the space charge density depends entirely on the spatiotemporal voltage distribution. Therefore, if the spatiotemporal voltage distribution can be determined analytically, the spatiotemporal evolution equation of the space-charge density can be obtained. Based on the analysis strategy described in previous studies [21,79], the Nernst–Planck equations can be used to describe this dynamic process.

$$\frac{\partial \tilde{c}_i}{\partial \tilde{t}} = \tilde{\nabla} \cdot (\tilde{D}_i \tilde{\nabla} \tilde{c}_i + \tilde{D}_i \tilde{z}_i \tilde{c}_i \tilde{\nabla} \tilde{\varphi}), \quad (\text{A1})$$

$$-\tilde{\nabla}^2 \tilde{\varphi} = \frac{\tilde{z}_1 \tilde{c}_1 + \tilde{z}_2 \tilde{c}_2}{\tilde{\lambda}_D^2}. \quad (\text{A2})$$

A one-dimensional transport process for salt solutions with a unit valence and equal diffusion coefficients is considered. Therefore, Eqs. (A1) and (A2) can be simplified as

$$\frac{\partial \tilde{c}_1}{\partial \tilde{t}} = \frac{d^2 \tilde{c}_1}{d\tilde{x}^2} + \frac{d}{d\tilde{x}} \left(\tilde{c}_1 \frac{d\tilde{\varphi}}{d\tilde{x}} \right), \quad (\text{A3})$$

$$\frac{\partial \tilde{c}_2}{\partial \tilde{t}} = \frac{d^2 \tilde{c}_2}{d\tilde{x}^2} - \frac{d}{d\tilde{x}} \left(\tilde{c}_2 \frac{d\tilde{\varphi}}{d\tilde{x}} \right), \quad (\text{A4})$$

$$\frac{d^2 \tilde{\varphi}}{d\tilde{x}^2} = \frac{\tilde{c}_1 - \tilde{c}_2}{\tilde{\lambda}_D^2}. \quad (\text{A5})$$

The following variables are introduced to facilitate subsequent discussions:

$$\tilde{c} = \tilde{c}_1 + \tilde{c}_2, \quad (\text{A6})$$

$$\tilde{q} = \tilde{c}_1 - \tilde{c}_2, \quad (\text{A7})$$

$$\tilde{E} = -\frac{d\tilde{\varphi}}{d\tilde{x}}, \quad (\text{A8})$$

where \tilde{c} represents the concentration, \tilde{q} is the charge, and \tilde{E} denotes the electric field. On substituting Eqs. (A6)–(A8) into Eqs. (A3)–(A5), we obtain

$$\frac{\partial \tilde{c}}{\partial \tilde{t}} = \frac{d^2 \tilde{c}}{d\tilde{x}^2} - \frac{d(\tilde{q}\tilde{E})}{d\tilde{x}}, \quad (\text{A9})$$

$$\frac{\partial \tilde{q}}{\partial \tilde{t}} = \frac{d^2 \tilde{q}}{d\tilde{x}^2} - \frac{d(\tilde{c}\tilde{E})}{d\tilde{x}}. \quad (\text{A10})$$

Substituting Poisson's Eq. (A5) into Eqs. (A9) and (A10) yields

$$\frac{\partial \tilde{c}}{\partial \tilde{t}} = \frac{d^2 \tilde{c}}{d\tilde{x}^2} - \frac{1-\tilde{z}}{2\tilde{\lambda}_D^2} \frac{d^2(\tilde{E}^2)}{d\tilde{x}^2}, \quad (\text{A11})$$

$$\tilde{\lambda}_D^{-2} \frac{d(d\tilde{E}/d\tilde{x})}{d\tilde{t}} = \tilde{\lambda}_D^{-2} \frac{d^3 \tilde{E}}{d\tilde{x}^3} - \frac{d(\tilde{c}\tilde{E})}{d\tilde{x}}. \quad (\text{A12})$$

On integrating Eq. (A12), we can obtain

$$-\tilde{\lambda}_D^{-2} \left(\frac{d\tilde{E}}{d\tilde{t}} - \frac{d^2 \tilde{E}}{d\tilde{x}^2} \right) = \tilde{c}\tilde{E} + \text{const}. \quad (\text{A13})$$

When $\tilde{\lambda}_D$ is very small, $-\tilde{\lambda}_D^{-2} \left(\frac{d\tilde{E}}{d\tilde{t}} - \frac{d^2 \tilde{E}}{d\tilde{x}^2} \right)$ can be neglected. Therefore, the physical interpretation of *const* is that the ion current crosses the membrane interface. We have *const* = \tilde{j} . For a single cation-selective membrane, the limiting current density ($\tilde{j}_{\text{limiting}}$) is 1.

In the early stages, we consider a scenario with only two regions: the EDL and the diffuse layer. In the latter, we consider the expansion of the electric field as follows:

$$\tilde{E}_{DL} \approx \tilde{E}_{DL,0} + \tilde{\lambda}_D \tilde{E}_{DL,1} + \tilde{\lambda}_D^2 \tilde{E}_{DL,2} + \dots, \quad (\text{A14})$$

where \tilde{E}_{DL} is the electric field intensity of the diffuse layer, and the distributions of $\tilde{E}_{DL,0}$, $\tilde{E}_{DL,1}$, and $\tilde{E}_{DL,2}$ are the electric field solutions of the zero-, first-, and second-order expansions, respectively. It can be observed from Poisson's equation that the space charge satisfies $\tilde{q} \sim O(\tilde{\lambda}_D^2)$. Therefore, under the limit of a small $\tilde{\lambda}_D$, Eqs. (A11) and (A12) can be simplified as follows:

$$\frac{\partial \tilde{c}_{DL}}{\partial \tilde{t}} = \frac{d^2 \tilde{c}_{DL}}{d\tilde{x}^2} - \frac{1-\tilde{\gamma}_D}{2^{\lambda_D}} \frac{d^2 (\tilde{E}_{DL})^2}{d\tilde{x}^2}, \quad (\text{A15})$$

$$\tilde{\gamma}_D \frac{d(d\tilde{E}_{DL}/d\tilde{x})}{d\tilde{t}} = \tilde{\gamma}_D \frac{d^3 \tilde{E}_{DL}}{d\tilde{x}^3} - \frac{d(\tilde{c}_{DL} \tilde{E}_{DL})}{d\tilde{x}}. \quad (\text{A16})$$

On solving the analytical solutions of Eqs. (A15) and (A16) [80], we can obtain the concentration distribution ($\tilde{c}_{DL}(\tilde{x}, \tilde{t})$) of the diffuse layer:

$$\tilde{c}_{DL}(\tilde{x}, \tilde{t}) = 1 - \tilde{j}(1 - \tilde{x}) - 2 \sum_{m=1}^{\infty} \frac{(-1)^m}{r_m^2} e^{-r_m^2 \tilde{t}} \sin[r_m(1 - \tilde{x})]. \quad (\text{A17})$$

Here, the eigenvalue r_m is $\pi(m - 1/2)$. Therefore, in the diffuse layer, the space-time distribution of the voltage is

$$\tilde{\varphi}_{DL}(\tilde{x}, \tilde{t}) = \int_{\tilde{\lambda}_D}^{\tilde{x}} \frac{d\tilde{\varphi}}{d\tilde{x}} d\tilde{x} = - \int_{\tilde{\lambda}_D}^{\tilde{x}} \tilde{E}_{DL,0} d\tilde{x} = \int_{\tilde{\lambda}_D}^{\tilde{x}} \frac{\tilde{j}}{\tilde{c}_{DL}(\tilde{x}, \tilde{t})} d\tilde{x}. \quad (\text{A18})$$

Then, for the diffuse layer ($\tilde{\lambda}_D < \tilde{x} < 1$), the space charge distribution is as follows:

$$\tilde{q}_{DL}(\tilde{x}, \tilde{t}) = -\tilde{\gamma}_D \frac{d^2 \tilde{\varphi}_{DL}(\tilde{x}, \tilde{t})}{d\tilde{x}^2} = -\tilde{\gamma}_D \frac{d^2 \left[\int_{\tilde{\lambda}_D}^{\tilde{x}} \frac{\tilde{j}}{\tilde{c}_{DL}(\tilde{x}, \tilde{t})} d\tilde{x} \right]}{d\tilde{x}^2}. \quad (\text{A19})$$

In the EDL ($0 < \tilde{x} < \tilde{\lambda}_D$), according to the electrochemical potential,

$$\tilde{\mu} = \ln(\tilde{c}_1) + \tilde{\varphi}. \quad (\text{A20})$$

We can obtain the voltage distribution

$$\tilde{\varphi} = \tilde{\mu} - \ln(\tilde{c}_1(\tilde{x}, \tilde{t})). \quad (\text{A21})$$

Therefore, in the EDL ($0 < \tilde{x} < \tilde{\lambda}_D$), the spatiotemporal distribution of the voltage mainly depends on the concentration, and we obtain

$$\tilde{\varphi}_{EDL}(\tilde{x}, \tilde{t}) = \ln \left[\frac{N}{\tilde{c}_{DL}(\tilde{x}, \tilde{t})} \right]. \quad (\text{A22})$$

Based on the above analysis, the space-time distribution of space charge in the double layer ($0 < \tilde{x} < \tilde{\lambda}_D$) is

$$\tilde{q}_{EDL}(\tilde{x}, \tilde{t}) = -\tilde{\gamma}_D \frac{d^2 \tilde{\varphi}_{EDL}(\tilde{x}, \tilde{t})}{d\tilde{x}^2} = -\tilde{\gamma}_D \frac{d^2 \ln \left[\frac{N}{\tilde{c}_{DL}(\tilde{x}, \tilde{t})} \right]}{d\tilde{x}^2}, \quad (\text{A23})$$

where N is the cation concentration at the nanoslot-bulk interface, which can be extracted from the direct numerical simulation data. The cation concentration at the outer edge of the EDL was assumed to be approximately equal to that at the edge of the diffuse layer. Therefore, Eqs. (A19) and (A23) can approximately describe the self-similar evolution law of the space charge in a short time.

Subsequently, the ESC forms, and with the progression of time, the ESC structure undergoes parallel expansion. From Eqs. (A11)–(A13), it can be inferred that, at this intermediate moment, the spatiotemporal distribution of the ESC can be described by the following equation:

$$\frac{\partial \tilde{c}_{ESC}}{\partial \tilde{t}} = \frac{d^2 \tilde{c}_{ESC}}{d\tilde{x}^2} - \frac{1-\tilde{\gamma}_D}{2^{\lambda_D}} \frac{d^2 (\tilde{E}_{ESC})^2}{d\tilde{x}^2}, \quad (\text{A24})$$

$$-\tilde{\gamma}_D \left(\frac{d\tilde{E}_{ESC}}{d\tilde{t}} - \frac{d^2 \tilde{E}_{ESC}}{d\tilde{x}^2} \right) = \tilde{c}_{ESC} \tilde{E}_{ESC} + \tilde{j}. \quad (\text{A25})$$

The space-charge layer comprises an ESC layer and a diffuse layer. Consequently, the overall voltage decrease across the entire system primarily comprises the voltage of the extended space charge and that of the diffuse layer. Thus, the spatiotemporal distribution of the voltage within the extended space charge ($0 < \tilde{x} < \tilde{x}_{ESC}$) can be derived, where \tilde{x}_{ESC} denotes the transient position.

$$\tilde{\varphi}_{ESC}(\tilde{x}, \tilde{t}) = \int_0^{\tilde{x}} \frac{\sqrt{\tilde{j}(\tilde{x}_{ESC} - \tilde{x})}}{\tilde{\lambda}_D} d\tilde{x} = \frac{2\sqrt{\tilde{j}}}{3\tilde{\lambda}_D} \left[(\tilde{x}_{ESC})^{\frac{3}{2}} - (\tilde{x}_{ESC} - \tilde{x})^{\frac{3}{2}} \right], \quad (\text{A26})$$

where \tilde{x}_{ESC} is a function of time, such that $\tilde{\varphi}_{ESC}(\tilde{x}, \tilde{t})$ is a function of time and position.

Similarly, for the diffuse layer ($\tilde{x}_{ESC} < \tilde{x} < 1$), we can obtain the spatio-temporal distribution of the voltage in the diffuse layer $\tilde{\varphi}_{DL1}(\tilde{x}, \tilde{t})$ during the intermediate time

$$\tilde{\varphi}_{DL1}(\tilde{x}, \tilde{t}) = \int_{\tilde{x}_{ESC}}^{\tilde{x}} \frac{\tilde{j}}{\tilde{c}_{DL}(\tilde{x}, \tilde{t})} d\tilde{x}. \quad (\text{A27})$$

Based on the above analysis, the spatiotemporal evolution of the voltage at an intermediate moment depends on the ESC position. At the edge of the

ESC (\tilde{x}_{ESC}), the ion concentration is approximately zero. The spatiotemporal changes in the ESC edge (\tilde{x}_{ESC}) can be deduced from the thickness of the diffuse layer as follows:

$$1 - \tilde{j}(1 - \tilde{x}_{ESC}) - 2 \sum_{m=1}^{\infty} \frac{(-1)^m}{r_m^2} e^{-r_m^2 \tilde{t}} \sin[r_m(1 - \tilde{x}_{ESC})] = 0. \tag{A28}$$

Therefore, we obtain

$$\tilde{x}_{ESC}(\tilde{t}) = 1 - \frac{1}{\tilde{j}} + \frac{2}{\tilde{j}} \sum_{m=1}^{\infty} \frac{(-1)^m}{r_m^2} e^{-r_m^2 \tilde{t}} \sin[r_m(1 - \tilde{x}_{ESC}(\tilde{t}))]. \tag{A29}$$

It should be noted that, in the analysis herein, for a single cation membrane, the ion flux is greater than the limiting current density (the value is 1). Therefore, we can obtain the spatiotemporal evolution law of the space-charge layer in the intermediate time.

For the diffuse layer ($\tilde{x}_{ESC} < \tilde{x} < 1$), the $\tilde{q}_{DL1}(\tilde{x}, \tilde{t})$ is

$$\tilde{q}_{DL1}(\tilde{x}, \tilde{t}) = -\tilde{\lambda}_D^{-2} \frac{d^2 \left[\int_{\tilde{x}_{ESC}}^{\tilde{x}} \frac{\tilde{j}}{2c_{DL}(x,t)} d\tilde{x} \right]}{d\tilde{x}^2}. \tag{A30}$$

For the ESC layer ($0 < \tilde{x} < \tilde{x}_{ESC}$), the $\tilde{q}_{ESC}(\tilde{x}, \tilde{t})$ is

$$\tilde{q}_{ESC}(\tilde{x}, \tilde{t}) = -\tilde{\lambda}_D^{-2} \frac{d^2 \tilde{\varphi}_{ESC}(\tilde{x}, \tilde{t})}{d\tilde{x}^2} = -\frac{\tilde{\lambda}_D \sqrt{\tilde{j}}}{2\tilde{\lambda}_D} (\tilde{x}_{ESC}(\tilde{t}) - \tilde{x})^{-1/2}. \tag{A31}$$

When the ESC is fully developed, the space-charge layer reaches a steady state. Using the Poisson–Nernst–Planck equations, it is expected that the decay scaling associated with the ESC Donnan potential can be derived theoretically. We consider the steady and non-convective Nernst–Planck equations, which yield

$$0 = \tilde{\nabla} \cdot (\tilde{\nabla} \tilde{c}_i + \tilde{z}_i \tilde{c}_i \tilde{\nabla} \tilde{\varphi}). \tag{A32}$$

Considering the horizontal transport of ions, cations undergo transport at the nanoslot-bulk interface, while anions are impeded at the nanoslot-bulk interface owing to the influence of the Donnan potential, thus giving nanoslots ion-selective characteristics. In the case of the negatively charged nanoslot in this study, the overall flux of the system mainly relies on the flux of the predominant cations, denoted as \tilde{j}_1 , while the flux of the anions \tilde{j}_2 is zero. For a symmetric and binary electrolyte ($\tilde{z}_1 = -\tilde{z}_2 = 1$), Eq. (A32) can be expressed as

$$\begin{aligned} \tilde{j}_1 &= \frac{d\tilde{c}_1}{d\tilde{x}} + \tilde{c}_1 \frac{d\tilde{\varphi}}{d\tilde{x}}, \\ 0 &= \frac{d\tilde{c}_2}{d\tilde{x}} - \tilde{c}_2 \frac{d\tilde{\varphi}}{d\tilde{x}}. \end{aligned} \tag{A33}$$

By adding these two equations to Eq. (A33), we obtain the transport equation for the salt concentration ($\tilde{c}_1 + \tilde{c}_2$):

$$\tilde{j}_1 = \frac{d(\tilde{c}_1 + \tilde{c}_2)}{d\tilde{x}} + \frac{d\tilde{\varphi}}{d\tilde{x}} (\tilde{c}_1 - \tilde{c}_2). \tag{A34}$$

Based on $-\frac{d^2 \tilde{\varphi}}{d\tilde{x}^2} = \frac{(\tilde{c}_1 - \tilde{c}_2)}{\tilde{\lambda}_D}$, Eq. (A34) can be rewritten as

$$\tilde{j}_1 = \frac{d(\tilde{c}_1 + \tilde{c}_2)}{d\tilde{x}} - \tilde{\lambda}_D^{-2} \frac{d\tilde{\varphi}}{d\tilde{x}} \frac{d^2 \tilde{\varphi}}{d\tilde{x}^2}. \tag{A35}$$

On letting $-\tilde{\lambda}_D \frac{d\tilde{\varphi}}{d\tilde{x}} = \tilde{E}_1$ and integrating Eq. (A35) once, we obtain the expression ($\tilde{c}_1 + \tilde{c}_2$):

$$\tilde{c}_1 + \tilde{c}_2 = \tilde{j}_1 (\tilde{x} - \tilde{x}_0) + \frac{1}{2} \tilde{E}_1^2. \tag{A36}$$

Eq. (A36) indicates that the salt concentration ($\tilde{c}_1 + \tilde{c}_2$) increases with the distance from the nanoslot-bulk interface. On subtracting the two equations from Eq. (A33), we obtain the transport equation for the charge ($\tilde{c}_1 - \tilde{c}_2$):

$$\tilde{j}_1 = \frac{d(\tilde{c}_1 - \tilde{c}_2)}{d\tilde{x}} + \frac{d\tilde{\varphi}}{d\tilde{x}} (\tilde{c}_1 + \tilde{c}_2). \tag{A37}$$

On substituting $-\frac{d^2 \tilde{\varphi}}{d\tilde{x}^2} = \frac{(\tilde{c}_1 - \tilde{c}_2)}{\tilde{\lambda}_D}$ and Eq. (A36) into Eq. (A37), we obtain

$$\tilde{j}_1 = \frac{d(\tilde{c}_1 - \tilde{c}_2)}{d\tilde{x}} + \frac{d\tilde{\varphi}}{d\tilde{x}} (\tilde{c}_1 + \tilde{c}_2) = \frac{d \left(-\tilde{\lambda}_D^{-2} \frac{d^2 \tilde{\varphi}}{d\tilde{x}^2} \right)}{d\tilde{x}} + \frac{d\tilde{\varphi}}{d\tilde{x}} \left(\tilde{j}_1 (\tilde{x} - \tilde{x}_0) + \frac{1}{2} \tilde{E}_1^2 \right). \tag{A38}$$

On multiplying both sides of Eq. (A38) by the dimensionless Debye number, we obtain

$$\tilde{\lambda}_D \tilde{j}_1 = \tilde{\lambda}_D \frac{d \left(-\tilde{\lambda}_D^{-2} \frac{d^2 \tilde{\varphi}}{d\tilde{x}^2} \right)}{d\tilde{x}} + \tilde{\lambda}_D \frac{d\tilde{\varphi}}{d\tilde{x}} \left[\tilde{j}_1 (\tilde{x} - \tilde{x}_0) + \frac{1}{2} \tilde{E}_1^2 \right]. \tag{A39}$$

Taking into consideration $-\tilde{\lambda}_D \frac{d\tilde{\varphi}}{d\tilde{x}} = \tilde{E}_1$, we can derive

$$\tilde{\lambda}_D \tilde{j}_1 = \tilde{\lambda}_D^2 \frac{d^2 \tilde{E}_1}{d\tilde{x}^2} - \tilde{E}_1 \left[\tilde{j}_1 (\tilde{x} - \tilde{x}_0) + \frac{1 - \tilde{x}^2}{2} \right]. \tag{A40}$$

The physical parameters satisfy $\tilde{E}_1 = O(1/\tilde{\lambda}_D)$ and $\frac{d}{d\tilde{x}} = O(1)$, and as $\tilde{\lambda}_D$ approaches zero, Eq. (A40) can be approximated as an algebraic equation:

$$\tilde{E}_1 \left[\tilde{j}_1 (\tilde{x} - \tilde{x}_0) + \frac{1 - \tilde{x}^2}{2} \right] = 0. \tag{A41}$$

We note that Eq. (A41) has a highly non-zero solution, which corresponds to the electric field in the ESC layer. We thus obtain

$$\tilde{\lambda}_D \frac{d\tilde{\varphi}}{d\tilde{x}} = \sqrt{2\tilde{j}_1 (\tilde{x}_0 - \tilde{x})} \text{ for } 0 < \tilde{x} < \tilde{x}_0. \tag{A42}$$

Eq. (A42) describes the electric field distribution within the ESC layer, where the electric field rapidly decays to zero far from the nanoslot-bulk interface, indicating a small electric field in the bulk region. Integrating Eq. (A42) yields the voltage distribution within the ESC layer:

$$\tilde{\varphi} = \left(\tilde{\lambda}_D^{-1} \sqrt{2\tilde{j}_1} \right) \cdot \left(\frac{2}{3} \right) \cdot \left[-(\tilde{x}_0 - \tilde{x})^{\frac{3}{2}} \right] + C \text{ for } 0 < \tilde{x} < \tilde{x}_0, \tag{A43}$$

where C is an integration constant. Considering the presence of the Donnan potential at $\tilde{x} = 0$, we can assume that the Donnan potential is $\tilde{\varphi}(\tilde{x} = 0) = \tilde{\varphi}_{Donnan}$. At $\tilde{x} = 1$, the voltage is $\tilde{\varphi}(\tilde{x} = 1) = \Delta\tilde{\varphi}$, where $\Delta\tilde{\varphi}$ represents the voltage at the anode induced by ion flux, and the voltage at the far left end of the channel is zero. The voltage at the edge of the ESC layer at $\tilde{\varphi}(\tilde{x} = \tilde{x}_0) = \tilde{\varphi}_0$. From Eq. (A43), we obtain the voltage decrease within the ESC layer $\tilde{\varphi}_0 - \tilde{\varphi}_{Donnan} = \left(\tilde{\lambda}_D^{-1} \sqrt{2\tilde{j}_1} \right) \cdot \left(\frac{2}{3} \right) \cdot (\tilde{x}_0)^{\frac{3}{2}}$. Hence, we can determine the expression for the integration constant \tilde{x}_0 , which represents the physical thickness of the ESC layer.

$$\tilde{x}_0 = \frac{\sqrt[3]{9} \cdot \frac{2}{3}}{2 \tilde{\lambda}_D^{\frac{2}{3}} (\tilde{j}_1)^{\frac{1}{3}}} (\tilde{\varphi}_0 - \tilde{\varphi}_{Donnan})^{2/3}. \tag{A44}$$

From Eq. (A44), it can be observed that, as the Donnan potential increases, the thickness of the ESC layer decreases. In particular, when the Donnan potential equals the potential at the edge of the ESC layer, the extended space charge layer disappears. It should be noted that the electric field intensity in the diffuse region is nearly zero, indicating that the voltage decrease across the entire anodic diffuse region can be approximated as equal to the anode voltage. Therefore, we obtain

$$\tilde{x}_0 = \frac{\sqrt[3]{9} \cdot \frac{2}{3}}{2 \tilde{\lambda}_D^{\frac{2}{3}} (\tilde{j}_1)^{\frac{1}{3}}} (\Delta\tilde{\varphi} - \tilde{\varphi}_{Donnan})^{2/3}. \tag{A45}$$

Furthermore, on substituting Eq. (A43) into the expression $-\frac{d^2 \tilde{\varphi}}{d\tilde{x}^2} = \frac{(z_1 c_1 - z_2 c_2)}{\tilde{\lambda}_D}$, we obtain the charge density within the ESC layer.

$$\tilde{c}_1 - \tilde{c}_2 = \tilde{\lambda}_D \cdot \sqrt{\frac{\tilde{j}_1}{2}} \cdot [\tilde{x}_0 - \tilde{x}]^{-\frac{1}{2}} \text{ for } 0 < \tilde{x} < \tilde{x}_0. \tag{A46}$$

However, for the diffusion region, the leading solution of $\frac{d\tilde{\varphi}}{d\tilde{x}}$ is given as [80]

$$\frac{d\tilde{\varphi}}{d\tilde{x}} = -\frac{1}{\tilde{x} - \tilde{x}_0} \text{ for } \tilde{x}_0 < \tilde{x} < 1. \tag{A47}$$

Therefore, we can obtain the charge density within the diffuse layer as follows:

$$\tilde{c}_1 - \tilde{c}_2 = \tilde{z}^{-1} \cdot \tilde{\lambda}_D^2 \left(\frac{1}{\tilde{x} - \tilde{x}_0} \right)^2 \text{ for } \tilde{x}_0 < \tilde{x} < 1. \tag{A48}$$

Finally, we obtain the space charge layer related to the Donnan potential as follows:

$$\begin{aligned} \tilde{c}_1 - \tilde{c}_2 &= \left(\frac{\tilde{j}_1}{2} \right)^{1/2} \cdot \tilde{\lambda}_D \cdot \left[\frac{\sqrt[3]{9} \cdot \frac{2}{3}}{2 \tilde{\lambda}_D^{\frac{2}{3}} (\tilde{j}_1)^{\frac{1}{3}}} (\Delta\tilde{\varphi} - \tilde{\varphi}_{Donnan})^{\frac{2}{3}} - \tilde{x} \right]^{-1/2} \text{ for ESC layer} \\ \tilde{c}_1 - \tilde{c}_2 &= \tilde{\lambda}_D^2 \cdot \left[\frac{\sqrt[3]{9} \cdot \frac{2}{3}}{2 \tilde{\lambda}_D^{\frac{2}{3}} (\tilde{j}_1)^{\frac{1}{3}}} (\Delta\tilde{\varphi} - \tilde{\varphi}_{Donnan})^{\frac{2}{3}} - \tilde{x} \right]^{-2} \text{ for diffuse layer} \end{aligned} \tag{A49}$$

The thickness of the ESC layer satisfies the relation $\tilde{x}_0 = \frac{\sqrt[3]{9} \cdot \frac{2}{3}}{2 \tilde{\lambda}_D^{\frac{2}{3}} (\tilde{j}_1)^{\frac{1}{3}}} (\Delta\tilde{\varphi} - \tilde{\varphi}_{Donnan})^{2/3}$. Therefore, for different voltage values, the position of the ESC layer changes. To normalize the position of the ESC layer, we use $\tilde{x} / \left[\frac{\sqrt[3]{9} \cdot \frac{2}{3}}{2 \tilde{\lambda}_D^{\frac{2}{3}} (\tilde{j}_1)^{\frac{1}{3}}} (\Delta\tilde{\varphi} - \tilde{\varphi}_{Donnan})^{2/3} \right]$ as the abscissa. The equations for the space charge density are as follows:

$$\tilde{c}_1 - \tilde{c}_2 \sim (\tilde{j}_1)^{1/2} \cdot \tilde{\lambda}_D \cdot \left[\tilde{x}_{ou} - \tilde{x} / \left(\frac{\sqrt[3]{9} \cdot 2}{2 \cdot \tilde{\lambda}_D^2 (\tilde{j}_1)^{-1/3}} (\Delta\tilde{\varphi} - \tilde{\varphi}_{Donnan})^{2/3} \right) \right]^{-1/2} \quad \text{for ESC layer} \quad (A50)$$

$$\tilde{c}_1 - \tilde{c}_2 \sim \tilde{\lambda}_D^2 \cdot \left[\tilde{x}_{ou} - \tilde{x} / \left(\frac{\sqrt[3]{9} \cdot 2}{2 \cdot \tilde{\lambda}_D^2 (\tilde{j}_1)^{-1/3}} (\Delta\tilde{\varphi} - \tilde{\varphi}_{Donnan})^{2/3} \right) \right]^{-2} \quad \text{for diffuse layer} \quad (A51)$$

This collapses the structure of the space charge layer curve near the theoretical curve, thus allowing us to obtain the normalized thickness of the space charge layer \tilde{x}_{ou} , which is approximately 0.52. Using the normalized thickness of the ESC layer \tilde{x}_{ou} , the universal distribution of the space charge density can be obtained, as shown in Fig. 6(a) and (b).

Data availability

Data will be made available on request.

References

- [1] Savage N, Diallo MS. Nanomaterials and water purification: opportunities and challenges. *J Nanoparticle Res* 2005;7(4):331–42.
- [2] Ramachandran A, Hemmatifar A, Hawks SA, Stadermann M, Santiago JG. Self similarities in desalination dynamics and performance using capacitive deionization. *Water Res* 2018;140:323–34.
- [3] Oyarzun DI, Hemmatifar A, Palko JW, Stadermann M, Santiago JG. Ion selectivity in capacitive deionization with functionalized electrode: theory and experimental validation. *Water Res X* 2018;1:100008.
- [4] Suss ME, Baumann TF, Bourcier WL, Spadaccini CM, Rose KA, Santiago JG, et al. Capacitive desalination with flow-through electrodes. *Energy Environ Sci* 2012;5(11):9511–9.
- [5] Pulkova NV, Zyrina AN, Mnafki NA, Kuznetsova IM. Microfluidic chip as a tool for effective in vitro evaluation of cyclophosphamide prodrug toxicity. *Bull Exp Biol Med* 2022;173(1):146–50.
- [6] Xuan XC, Li DQ. Focused electrophoretic motion and selected electrokinetic dispensing of particles and cells in cross-microchannels. *Electrophoresis* 2005;26(18):3552–60.
- [7] Daghighi Y, Li DQ. Numerical study of a novel induced-charge electrokinetic micro-mixer. *Anal Chim Acta* 2013;763:28–37.
- [8] Peng R, Li DQ. Effects of ionic concentration gradient on electroosmotic flow mixing in a microchannel. *J Colloid Interface Sci* 2015;440:126–32.
- [9] Feng H, Chang H, Zhong X, Wong TN. Recent advancement in induced-charge electrokinetic phenomena and their micro- and nano-fluidic applications. *Adv Colloid Interface Sci* 2020;280:102159.
- [10] Erickson D, Li DQ. Integrated microfluidic devices. *Anal Chim Acta* 2004;507(1):11–26.
- [11] Alizadeh A, Hsu W-L, Wang M, Daiguji H. Electroosmotic flow: from microfluidics to nanofluidics. *Electrophoresis* 2021;42(7-8):834–68.
- [12] Lebègue E. Electrochemical methods: fundamentals and applications, 3rd edition. *Transit MetChem* 2023;48(6):433–6.
- [13] Bernèche S, Roux B. Energetics of ion conduction through the K^+ channel. *Nature* 2001;414(6859):73–7.
- [14] Deng D, Dydek EV, Han J-H, Schlumpberger S, Mani A, Zaltzman B, et al. Overlimiting current and shock electro dialysis in porous media. *Langmuir* 2013;29(52):16167–77.
- [15] Deng D, Aouad W, Braff WA, Schlumpberger S, Suss ME, Bazant MZ. Water purification by shock electro dialysis: deionization, filtration, separation, and disinfection. *Desalination* 2015;357:77–83.
- [16] Lin C-Y, Hsu J-P, Yeh L-H. Rectification of ionic current in nanopores functionalized with bipolar polyelectrolyte brushes. *Sensor Actuat B-Chem* 2018;258(1):1223–9.
- [17] Alizadeh A, Hsu W-L, Daiguji H, Wang M. Temperature-regulated surface charge manipulates ionic current rectification in tapered nanofluidic channel. *Int J Mech Sci* 2021;210(15):106754.
- [18] Warren P. Metrology - Electrifying effects in colloids. *Nature* 2004;429(6994):822–22.
- [19] Squires TM, Quake SR. Microfluidics: fluid physics at the nanoliter scale. *Rev Mod Phys* 2005;77(3):977–1026.
- [20] Stone HA, Stroock AD, Ajdari A. Engineering flows in small devices: microfluidics toward a lab-on-a-chip. *Annu Rev Fluid Mech* 2004;36:381–411.
- [21] Rubinstein I, Zaltzman B. Electro-osmotically induced convection at a permselective membrane. *Phys Rev E* 2000;62(2):2238.
- [22] Rubinstein I, Zaltzman B. Equilibrium electroconvective instability. *Phys Rev Lett* 2015;114(11):114502.
- [23] Xu B, Gu Z, Liu W, Huo P, Zhou Y, Rubinstein SM, et al. Electro-osmotic instability of concentration enrichment in curved geometries for an aqueous electrolyte. *Phys Rev Fluids* 2020;5(9):091701.
- [24] Bonhomme O, Peng L, Bianca A-L. Thermally enhanced electro-osmosis to control foam stability. *Phys Rev X* 2020;10(2).
- [25] Guan Y, Riley J, Novoselov I. Three-dimensional electroconvective vortices in cross flow. *Phys Rev E* 2020;101(3):033103.
- [26] Luo K, Wu J, Yi H-L, Tan H-P. Numerical analysis of two-phase electrohydrodynamic flows in the presence of surface charge convection. *Phys Fluids* 2020;32(12):123606.
- [27] Alizadeh A, Zhang L, Wang M. Mixing enhancement of low-Reynolds electro-osmotic flows in microchannels with temperature-patterned walls. *J Colloid Interface Sci* 2014;431(1):50–63.
- [28] Khair AS. Concentration polarization and second-kind electrokinetic instability at an ion-selective surface admitting normal flow. *Phys Fluids* 2011;23(7):072003.
- [29] Rubinstein I, Zaltzman B. Electro-osmotic slip of the second kind and instability in concentration polarization at electro dialysis membranes. *Math Models Methods Appl Sci* 2001;11(2):263–300.
- [30] Davidson SM, Andersen MB, Mani A. Chaotic induced-charge electro-osmosis. *Phys Rev Lett* 2014;112(12):128302.
- [31] Demekhin EA, Nikitin NV, Shelistov VS. Three-dimensional coherent structures of electrokinetic instability. *Phys Rev E* 2014;90(1):013031.
- [32] Karatay E, Andersen MB, Wessling M, Mani A. Coupling between Buoyancy Forces and Electroconvective Instability near Ion-Selective Surfaces. *Phys Rev Lett* 2016;116(19):194501.
- [33] Pham VS, Li Z, Lim KM, White JK, Han J. Direct numerical simulation of electroconvective instability and hysteretic current-voltage response of a permselective membrane. *Phys Rev E* 2012;86(4):046310.
- [34] Rubinstein SM, Manukyan G, Staicu A, Rubinstein I, Zaltzman B, Lammertink RGH, et al. Direct observation of a nonequilibrium electro-osmotic instability. *Phys Rev Lett* 2008;101(23):236101.
- [35] Yossifon G, Chang H-C. Selection of nonequilibrium overlimiting currents: universal depletion layer formation dynamics and vortex instability. *Phys Rev Lett* 2008;101(25):254501.
- [36] Demekhin EA, Nikitin NV, Shelistov VS. Direct numerical simulation of electrokinetic instability and transition to chaotic motion. *Phys Fluids* 2013;25(12):122001.
- [37] Demekhin EA, Amiroudine S, Ganchenko GS, Khasmatulina NY. Thermoelectroconvection near charge-selective surfaces. *Phys Review E* 2015;91(6):063006.
- [38] Druzgalski C, Mani A. Statistical analysis of electroconvection near an ion-selective membrane in the highly chaotic regime. *Phys Rev Fluids* 2016;1(7):073601.
- [39] Druzgalski CL, Andersen MB, Mani A. Direct numerical simulation of electroconvective instability and hydrodynamic chaos near an ion-selective surface. *Phys Fluids* 2013;25(11):110804.
- [40] Tizakast Y, Kaddiri M, Lamsaadi M. Rayleigh-Benard double-diffusive mixed convection in two-dimensional rectangular cavities filled with non-Newtonian fluids. *Int J Mech Sci* 2022:227.
- [41] Aghighi MS, Ammar A, Masoumi H, Lanjani A. Rayleigh-Benard convection of a viscoplastic liquid in a trapezoidal enclosure. *Int J Mech Sci* 2020:180.
- [42] Lakshmi KM, Siddheshwar PG, Muddamallappa MS. Study of rotating Benard-Brinkman convection of Newtonian liquids and nanoliquids in enclosures. *Int J Mech Sci* 2020:188.
- [43] Al-Rashed A, Oztop HF, Kolsi L, Boudjemline A, Almeshaal MA, Ali ME, et al. CFD study of heat and mass transfer and entropy generation in a 3D solar distiller heated by an internal column. *Int J Mech Sci* 2019;152:280–8.
- [44] Demekhin EA, Shelistov VS, Polyanskikh SV. Linear and nonlinear evolution and diffusion layer selection in electrokinetic instability. *Phys Rev E* 2011;84(3):036318.
- [45] Kwak R, Van Sang P, Lim KM, Han J. Shear flow of an electrically charged fluid by ion concentration polarization: scaling laws for electroconvective vortices. *Phys Rev Lett* 2013;110(11):114501.
- [46] Liu W, Zhou Y, Shi P. Shear electroconvective instability in electro dialysis channel under extreme depletion and its scaling laws. *Phys Rev E* 2020;101(4):043105.
- [47] Liu W, Zhou Y, Shi P. Scaling laws of electroconvective flow with finite vortex height near permselective membranes. *Phys Rev E* 2020;102(3):033102.
- [48] Kwak R, Van Sang P, Han J. Sheltering the perturbed vortical layer of electroconvection under shear flow. *J Fluid Mech* 2017;813(10):799–823.
- [49] Liu W, Zhou Y, Shi P. Critical selection of shear sheltering in electroconvective flow from chaotic to steady state. *J Fluid Mech* 2022;946(10):A3.
- [50] Kang S, Kwak R. Pattern formation of three-dimensional electroconvection on a charge selective surface. *Phys Rev Lett* 2020;124(15):154502.

- [51] Shi P, Liu W. Length-dependent instability of shear electroconvective flow: from electroconvective instability to rayleigh-benard instability. *J Appl Phys* 2018;124(20):204304.
- [52] Li G, Archer LA, Koch DL. Electroconvection in a viscoelastic electrolyte. *Phys Rev Lett* 2019;122(12):124501.
- [53] Cai J, Zhao D, Li G. Direct numerical simulation of electroconvection under a uniform magnetic field. *Phys Rev Fluids* 2023;8(11):113701.
- [54] Andersen MB, van Soestbergen M, Mani A, Bruus H, Biesheuvel PM, Bazant MZ. Current-induced membrane discharge. *Phys Rev Lett* 2012;109(10).
- [55] Gu Z, Xu B, Huo P, Rubinstein SM, Bazant MZ, Deng D. Deionization shock driven by electroconvection in a circular channel. *Phys Rev Fluids* 2019;4(11).
- [56] Sunil Sharma A, Bharti PK, Shandil RG. Linear stability of double-diffusive convection in a micropolar ferromagnetic fluid saturating a porous medium. *Int J Mech Sci* 2007;49(9):1047–59.
- [57] Abbassi MA, Safaei MR, Djebali R, Guedri K, Zeghami B, Alrashed A. LBM simulation of free convection in a nanofluid filled incinerator containing a hot block. *Int J Mech Sci* 2018;148:393–408.
- [58] Venkatadri K, Bég OA, Rajarajeswari P, Prasad VR. Numerical simulation of thermal radiation influence on natural convection in a trapezoidal enclosure: heat flow visualization through energy flux vectors. *Int J Mech Sci* 2020:171.
- [59] Gokturk PA, Sujanani R, Qian J, Wang Y, Katz LE, Freeman BD, et al. The donnan potential revealed. *Nat Commun* 2022;13(1):5880.
- [60] Tian H, Zhang L, Wang M. Applicability of Donnan equilibrium theory at nanochannel-reservoir interfaces. *J Colloid Interface Sci* 2015;452(15):78–88.
- [61] Mani A, Wang KM. Electroconvection near electrochemical interfaces: experiments, modeling, and computation. *Annu Rev Fluid Mech* 2020;52:509–29.
- [62] Tian H, Wang M. Electrokinetic mechanism of wettability alternation at oil-water-rock interface. *Surf Sci Rep* 2017;72(6):369–91.
- [63] Rubinstein I, Zaltzman B. Dynamics of extended space charge in concentration polarization. *Phys Rev E* 2010;81(6).
- [64] Lam ET, Hastie A, Lin C, Ehrlich D, Das SK, Austin MD, et al. Genome mapping on nanochannel arrays for structural variation analysis and sequence assembly. *Nat Biotechnol* 2012;30(8):771–6.
- [65] Nguyen DT, Pham V. Modeling non-linear ion transport phenomena in ion-selective membranes: three simplified models. *Sep Purif Technol* 2024;333.
- [66] Nakamura M, Kaminaga H, Endo O, Tajiri H, Sakata O, Hoshi N. Structural dynamics of the electrical double layer during capacitive charging/discharging processes. *J Phys ChemC* 2014;118(38):22136–40.
- [67] Jiang XK, Huang JS, Zhao H, Sumpter BG, Qiao R. Dynamics of electrical double layer formation in room-temperature ionic liquids under constant-current charging conditions. *J Phys Condens Matter* 2014;26(28).
- [68] Henrique F, Zuk PJ, Gupta A. Charging dynamics of electrical double layers inside a cylindrical pore: predicting the effects of arbitrary pore size. *Soft Matter* 2021;18(1):198–213.
- [69] Chandra A. Dynamics of electrical double layer formation at a charged solid surface. *J Mol Struct Theochem* 1998;430:105–11.
- [70] Mirzadeh M, Gibou F, Squires TM. Enhanced Charging kinetics of porous electrodes: surface conduction as a short-circuit mechanism. *Phys Rev Lett* 2014;113(9).
- [71] Pascall AJ, Squires TM. Electrokinetics at liquid/liquid interfaces. *J Fluid Mech* 2011;684:163–91.
- [72] Qiao R, Aluru NR. Ion concentrations and velocity profiles in nanochannel electroosmotic flows. *J Chem Phys* 2003;118(10):4692–701.
- [73] Xuan XC, Sinton D, Li DQ. Thermal end effects on electroosmotic flow in a capillary. *Int J Heat Mass Transf* 2004;47(14-16):3145–57.
- [74] Coquinot B, Bocquet L, Kavokine N. Quantum feedback at the solid-liquid interface: flow-induced electronic current and its negative contribution to friction. *Phys Rev X* 2023;13(1).
- [75] Keser AC, Wang DQ, Klochan O, Ho DYH, Tkachenko OA, Tkachenko VA, et al. Geometric control of universal hydrodynamic flow in a two-dimensional electron fluid. *Phys Rev X* 2021;11(3).
- [76] Uzdénova A. Time-dependent two-dimensional model of overlimiting mass transfer in electromembrane systems based on the nernst-planck, displacement current and navier-stokes equations. *Computation* 2023;11(10):205.
- [77] Daiguji H, Yang PD, Majumdar A. Ion transport in nanofluidic channels. *Nano Lett* 2004;4(1):137–42.
- [78] Green Y, Yossifon G. Dynamical trapping of colloids at the stagnation points of electro-osmotic vortices of the second kind. *Phys Rev E* 2013;87(3):033005.
- [79] Zaltzman B, Rubinstein I. Electro-osmotic slip and electroconvective instability. *J Fluid Mech* 2007;579(25):173–226.
- [80] Sístat P, Pourcelly G. Chronopotentiometric response of an ion-exchange membrane in the underlimiting current-range. Transport phenomena within the diffusion layers. *J Membr Sci* 1997;123(1):121–31.
- [81] Kamsma TM, Boon WQ, Rele TT, Spitoni C, van Roij R. Iontronic neuromorphic signaling with conical microfluidic memristors. *Phys Rev Lett* 2023;130(26).
- [82] Kamsma TM, Kim J, Kim K, Boon WQ, Spitoni C, Park J, et al. Brain-inspired computing with fluidic iontronic nanochannels. *Proc Natl Acad Sci U S A* 2024;121(18).
- [83] Noy A, Li ZW, Darling SB. Fluid learning: mimicking brain computing with neuromorphic nanofluidic devices. *Nano Today* 2023;53.
- [84] Ramirez P, Portillo S, Cervera J, Bisquert J, Mafe S. Memristive arrangements of nanofluidic pores. *Phys Rev E* 2024;109(4).
- [85] Miah MS, Amjady N, Shah R, Islam S. Energy recovery from polluted water using capacitive deionization desalination system: a review. *Ieee Access* 2024;12:110002–27.